
AICCA: AI-DRIVEN CLOUD CLASSIFICATION ATLAS

A PREPRINT

Takuya Kurihana*
Dept. of Computer Science
University of Chicago
Chicago, IL 60637
tkurihana@uchicago.edu

Elisabeth Moyer[†]
Dept. of the Geophysical Sciences
University of Chicago
Chicago, IL 60637
moyer@uchicago.edu

Ian Foster^{}**
Dept. of Computer Science
University of Chicago
Chicago, IL 60637
foster@uchicago.edu

October 3, 2022

ABSTRACT

Clouds play an important role in the Earth’s energy budget and their behavior is one of the largest uncertainties in future climate projections. Satellite observations should help in understanding cloud responses, but decades and petabytes of multispectral cloud imagery have to date received only limited use. This study reduces the dimensionality of satellite cloud observations by grouping them via a novel automated, unsupervised cloud classification technique by using a convolutional neural network. Our technique combines a rotation-invariant autoencoder with hierarchical agglomerative clustering to generate cloud clusters that capture meaningful distinctions among cloud textures, using only raw multispectral imagery as input. Thus, cloud classes are defined without reliance on location, time/season, derived physical properties, or pre-designated class definitions. We use this approach to generate a unique new cloud dataset, the AI-driven cloud classification atlas (AICCA), which clusters 22 years of ocean images from the Moderate Resolution Imaging Spectroradiometer (MODIS) on NASA’s Aqua and Terra instruments—800 TB of data or 198 million patches roughly 100 km × 100 km (128 × 128 pixels)—into 42 AI-generated cloud classes. We show that AICCA classes involve meaningful distinctions that employ spatial information and result in distinct geographic distributions, capturing, for example, stratocumulus decks along the West coasts of North and South America. AICCA delivers the information in multi-spectral images in a compact form, enables data-driven diagnosis of patterns of cloud organization, provides insight into cloud evolution on timescales of hours to decades, and helps democratize climate research by facilitating access to core data.

1 Introduction

Over the past several decades, advancements in satellite-borne remote sensing instruments have produced hundreds of terabytes of global multispectral imagery that captures cloud structure, size distributions, and radiative properties at a near-daily cadence. These datasets are underutilized because climate scientists cannot in practice manually examine these enormous datasets to analyze spatial-temporal patterns. Instead, some kind of automated algorithm is needed to identify cloud types that are relevant to climate science. However, the diversity of cloud morphologies and textures, and their multi-scale properties, makes classifying them into meaningful groupings a difficult task.

Existing classification schemes are necessarily simplistic. The most standard classification, the ISCCP (International Satellite Cloud Climatology Project) schema, simply defines a grid of nine global classes based on low, medium, or high values of cloud altitude (cloud top pressure) and optical thickness [Rossow and Schiffer \[1991\]](#), [Rossow et al. \[1993\]](#), [Rossow and Schiffer \[1999\]](#). Because this classification is typically applied pixel by pixel, it cannot capture spatial structures and can produce an incoherent spatial distribution of cloud types in cloud imagery. The World

*Globus Labs: <https://labs.globus.org/>

[†]The Center for Robust Decision-making on Climate and Energy Policy (RDCEP): <http://www.rdcep.org/>

[‡]Argonne National laboratory, The Data Science and Learning Division: <https://www.anl.gov/dsl>

Meteorological Organization’s International Cloud Atlas [World Meteorological Organization](#), a more complex cloud classification framework, defines 28 different classes (of which 10 are considered ‘basic types’) with a complex coding procedure that depends on subjective judgments, such as whether a cloud has yet “become fibrous or striated.” The schema is subjective and difficult to automate, and furthermore does not capture the full diversity of important cloud types. For example, it does not distinguish between open- and closed-cell stratocumulus clouds, placing them both in “stratocumulus,” though the two have different circulation patterns, rain rates, and radiative effects [Wood \[2012\]](#). Because the human eye serves as sensitive tool for pattern classification, human observers can in principle group clouds into a larger set of types based on texture and shape as well as altitude and thickness. In practice, however, it has been difficult to devise a set of artificial cloud categories that encompass all cloud observations and can be applied consistently by human labelers.

These issues motivate the application of artificial intelligence (AI)-based algorithms for cloud classification. In the last several years, a number of studies have sought to develop AI-based cloud classification by using *supervised learning* [Zhang et al. \[2018\]](#), [Rasp et al. \[2019\]](#), [Zantedeschi et al. \[2019\]](#), [Marais et al. \[2020\]](#). In these approaches, ML models are trained to classify cloud images based on a training set to which humans have assigned labels. However, the difficulty of generating meaningful and consistent labels is a constant problem, and supervised learning approaches tend to succeed best when used on limited datasets containing classic examples of well-known textures. For example, [Rasp et al. \[2019\]](#) classified just four particular patterns of stratocumulus defined and manually labeled by [Stevens et al. \[2020\]](#). Supervised methods cannot discover unknown cloud types that may be relevant to climate change research.

To serve the needs of climate research, the more appropriate choice is *unsupervised learning*, in which unknown patterns in data are learned without requiring predefined labels. The first demonstrations of unsupervised methods applied to cloud images were made in the 1990s [Visa et al. \[1998\]](#), [Tian et al. \[1999\]](#). Even with the primitive neural networks then available, [Tian et al. \[1999\]](#) showed that cloud images from the GOES-8 satellite could be sorted automatically into ten clusters that reproduced the ten ‘basic’ WMO classes with 65–75% accuracy. In 2019, [Denby \[2020\]](#) and [Kurihana et al. \[2019\]](#) leveraged advances in deep neural network (DNN) methods to prototype unsupervised cloud classification algorithms based on convolutional neural networks (CNNs), DNNs with convolutional layers. Both works used only 12 classes and neither was rotation-invariant, but both successfully produced reasonable-seeming classifications—for [Denby \[2020\]](#), from near-infrared images from the GOES satellite in the tropical Atlantic, and for [Kurihana et al. \[2019\]](#), from global multispectral images from the Moderate Resolution Imaging Spectroradiometer (MODIS) instruments on NASA’s Aqua and Terra satellites). [Kurihana et al. \[2021\]](#) extended the work to develop rotation-invariant cloud clustering (RICC), by using an autoencoder [Hinton et al. \[2011\]](#), a class of unsupervised DNNs widely used for dimensionality reduction, and applying hierarchical agglomerative clustering (HAC) [Johnson \[1967\]](#) to the compact representation generated by the autoencoder to produce cloud clusters, but adding a more complex loss function. [Kurihana et al. \[2021\]](#) also developed a formal evaluation protocol to judge if the resulting unsupervised cloud clustering generates results that are truly physically meaningful.

The work described here builds on these previous results to generate a standardized science product: an AI-driven Cloud Classification Atlas (AICCA) of global-scale unsupervised classification of MODIS satellite imagery into 42 cloud classes. We first describe and apply a protocol for determining the optimal number of clusters when applying RICC to the MODIS dataset, which we determine to be 42. We demonstrate that the resulting classes are coherent geographically, temporally, and in altitude-optical depth space. Finally, we describe a workflow that allows us to apply the RICC₄₂ algorithm to the full two decades of MODIS imagery to provide a publicly available dataset. The result is an automated, unsupervised classification process that discovers classes based on both cloud morphology and physical properties, and yields unbiased cloud classes free from artificial assumptions that capture the diversity of global cloud types. AICCA is intended to support studies of the response of clouds to forcing on timescales from hours to decades and to allow data-driven diagnosis of cloud organization and behavior and their evolution over time as CO₂ and temperatures increase.

We describe this dataset as follows. Section 2 describes the MODIS imagery, information used, and structure of output data. Section 3 describes the algorithm used for classification, including the training procedure on one million randomly selected ocean-cloud patches (Section 3.2). Section 4 evaluates the stability of the clustering step, and Section 5 describes the characteristics of the resulting cloud clusters: their distribution geographically, seasonally, and in altitude-optical depth space.

2 AICCA: data and outputs

The dataset described here, AICCA₄₂ (or simply AICCA), provides AI-generated cloud class labels for all ocean clouds sampled by MODIS instruments over their 22 years of operation. The cloud labels (range 1..42) are generated by the rotation-invariant cloud clustering (RICC) method of [Kurihana et al. \[2021\]](#) configured to generate 42 clusters, using

Table 1: MODIS products used to create the AICCA dataset. As noted in the text, each product name *MOD0X* in the first column refers to both the Aqua (MYD0X) and Terra (MOD0X) products. Source: NASA Earthdata.

Product	Description	Band	Primary Use	Process
MOD02	Shortwave infrared (1.230–1.250 μm)	5	Land/cloud/aerosol properties	Patch §3.1
	Shortwave infrared (1.628–1.652 μm)	6	Land/cloud/aerosol properties	
	Shortwave infrared (2.105–2.155 μm)	7	Land/cloud/aerosol properties	
	Longwave thermal infrared (3.660–3.840 μm)	20	Surface/cloud temperature	
	Longwave thermal infrared (7.175–7.475 μm)	28	Cirrus clouds water vapor	
	Longwave thermal infrared (8.400–8.700 μm)	29	Cloud properties	
	Longwave thermal infrared (10.780–11.280 μm)	31	Surface/cloud temperature	
MOD03	Geolocation fields	Latitude and Longitude		QC §3.1
MOD06	Cloud mask	Cloud pixel detection		
	Land / Water	Background detection		
	Cloud optical thickness	Thickness of cloud		Evaluation §3.3
	Cloud top pressure	Pressure at cloud top		
	Cloud phase infrared	Cloud particle phase		
	Cloud effective radius	Radius of cloud droplet		

input imagery subdivided into 128×128 pixel (~ 100 km by 100 km) *patches*. Clusters produced from RICC vary according to 1) the data used to train RICC, 2) the number of clusters chosen, and 3) the clustering centroids data that the trained RICC is applied to. Because there are high degrees of freedom that attribute to the selection of these three factors, we define AICCA that is produced from the combination of RICC₄₂ and a set of reference centroids based on OC-Patches_{HAC} defined in Section 4.4. The labeled output is provided in two different ways: as the original patches and resampled to $1^\circ \times 1^\circ$ grid cells.

2.1 MODIS Data

The MODIS instruments hosted on NASA’s Aqua and Terra satellites have been collecting visible to mid-infrared radiance data in 36 spectral bands from 2002 (Aqua) MODIS Characterization Support Team [2017b] and 2000 (Terra) MODIS Characterization Support Team [2017a] through 2021. The instruments collect data over an approximately 2330 km by 2030 km *swath* every five minutes, with a spatial resolution of 1 km. AICCA is based on the MODIS Level 1B calibrated radiance product (MOD02). (Note that while NASA uses the prefixes MOD and MYD to distinguish between Terra and Aqua, respectively, for simplicity we use MOD to refer to both throughout this article.) We limit the dataset to the 6 spectral bands most relevant for derivation of physical properties: bands 6, 7, and 20 relate to cloud optical properties, and bands 28, 29, and 31 relate to the separation of high and low clouds and the detection of the cloud phase. For the Aqua instrument, we use band 5 as an alternative to band 6 due to a known stripe noise issue in Aqua band 6 Rakwatin et al. [2007]. (See also Kurihana et al. [2021] for more details.) The total number of swath images per band is $(12 \text{ swath/hour}) \times (12 \text{ hour/day}) \times (365 \text{ day/year}) \times (20 + 22 \text{ years, for Aqua and Terra, respectively}) \approx 2.2$ million swathes, or a total of 13.2 million swathes across all bands used.

MODIS multispectral data are processed by NASA to yield a variety of products, and we use several others for post-processing or analysis. We use latitude and longitude from the MOD03 geolocation fields to regrid the AICCA patches, and use selected derived physical properties from the MOD06 product to evaluate the cloud classes: four physical parameters related to cloud optical properties and cloud top properties (CTP and CPI). Note that the MOD06 variables are used only as a diagnostic, to evaluate to what extent clustering results associate cloud physical properties in our clusters. They are not included in our RICC training data, so as to free from any assumptions imposed on these data. All data used in generating AICCA are listed in Table 1, and make up an aggregate size of 801 terabytes. All MODIS products are made available via the NASA Level-1 and Atmosphere Archive and Distribution System (LAADS), grouped into per-swath files.

2.2 AICCA Patch-Level Data

The AICCA dataset uses all patches from Aqua and Terra MODIS image data during 2000–2021, subject to the constraints that they are (a) disjoint in space and/or time; (b) include no non-ocean pixels, and (c) each include at least 30% cloud pixels. The resulting set is 198 676 800 individual 128×128 pixel (~ 100 km by 100 km) ocean-cloud

patches (numbered in first element of the AICCA₄₂ dataset). For each patch, AICCA₄₂ provides the information listed below and in Table 2, a total of 146 Bytes per patch, i.e. a factor of $16\,159 \times$ reduction relative to the raw multispectral imagery.

- Source is either Aqua or Terra;
- Swath, Location, and Timestamp locate the patch in time and space;
- Training indicates whether the patch was used for training;
- Label is an integer in the range 1..42, generated by the rotation-invariant cloud clustering system configured for 42 clusters, RICCA₄₂; and
- COT_patch, CTP_patch, and CER_patch: The mean and standard deviation, across all pixels in the patch, for three MOD06 physical values: cloud optical thickness (COT), cloud top pressure (CTP), and cloud effective radius (CER);
- CPI_patch: Cloud phase information (CPI), four numbers representing the number of the 128×128 pixels in the patch that are estimated as clear-sky, liquid, ice, or undefined, respectively.

The additional information shown in Table 2 that assists users in understanding each patch is easily extracted from MOD06 by using the patch’s geolocation index and timestamp (Location and Timestamp in Table 2) to locate the patch’s data in the appropriate MOD06 file. These mean values summarize the average physical characteristic for the patch; the standard deviations provide some indication as to the existence of multiple clouds (especially low- and high-altitude clouds). We do not use the MOD06 multilayered cloud flag.

Output is provided as NetCDF [R^ew and Davis \[1990\]](#) files that combine patches from each MODIS swath into a single file. While AICCA contains no raw satellite data, note that information for each patch in Table 2 includes an identifier for the source MODIS swath and a geolocation index, that allow users to link results with the original MOD02 satellite imagery and other MODIS products. The complete OC-Patches set contains around $(20 + 22 \text{ years}) \times (365 \text{ days/year}) \times (26\,000 \text{ patches}) \times 146 \text{ B} \approx 54.2 \text{ gigabytes}$.

2.3 AICCA Grid Cell-Level Data

In addition to providing per-patch data, we follow common practice in climate datasets by also providing data organized on a per-latitude/longitude grid cell basis. The second element of the AICCA₄₂ dataset spatially aggregates the patch-level class label and diagnostic values at a resolution of $1^\circ \times 1^\circ$, a total of 181×360 *grid cells* over the globe. For each resulting data item, AICCA₄₂ provides the information listed in Table 3, a total of 32 Bytes:

- Source is either Aqua or Terra;
- Cell gives a latitude and longitude for the grid cell;
- Timestamp locates the grid cell in time;
- Label_1deg represents the most frequent class label in the grid cell (an integer in the range 1..42); and
- COT_1deg, CTP_1deg, CER_1deg, and CPI_1deg aggregate values for four diagnostic variables, as described in Section 2.3.

The aggregation process uses values from individual days from the Aqua and Terra satellite, a reasonable choice since the MODIS instrument orbits the Earth about once per day. That is, the swaths taken by each satellite instrument generally do not overlap in a daily period. Since a single 2330 km by 2030 km MODIS swath extends across multiple 1 degree by 1 degree grid cells, we extract the latitude and longitude at the center of each OC-Patch by using MOD03, and aggregate the information listed in Table 2 to each $1^\circ \times 1^\circ$ grid cell (i.e., the area extending from -0.5° to $+0.5^\circ$ from the grid cell center). To assign a class label to each grid cell on each day, we use the class of the single ocean-cloud patch with the largest overlap with the grid cell. To provide physical properties for each grid cell, we do implement one simplification to reduce the use of computing memory: instead of averaging pixel values within each grid cell, we identify *all* ocean-cloud patches that overlap with the cell, and simply average those patches’ mean COT, CTP, and CER values. To assign a cloud particle phase (clear-sky, liquid, ice, or undefined) we use the most frequent phase in the overlapping patches. Grid cells with no clouds are labeled as a missing value.

In some cases, especially at high latitudes, swaths may overlap within a single day. When this occurs, patches with different timestamps will overlap a given grid cell on the same day. In these cases, we discard one timestamp, to avoid inconsistent values between grid cells. That is, when accumulating the most frequent label and aggregating values on the overlapping cell, we use only those patches with a timestamp close to that of the neighboring grid cells. This neighboring selection mitigates the problem of inconsistent values between nearby grid cells due only to timing.

Table 2: Information provided in AICCA for each 128×128 pixel ocean-cloud patch: metadata that locate the patch in space and time, and indicate whether the patch was used to train RICC; a cloud class label computed by RICC; and a set of diagnostic quantities obtained by aggregating MODIS data over all pixels in the patch.

Variables	Description	Values	Type
Swath	Identifier for source MODIS swath	1	float32
Location	Geolocation index for the upper left corner of patch	2	float32
Timestamp	Time of observation	1	float32
Training	Whether patch used for training	1	binary
Label	Class label assigned by RICC: integer in range $1..k^*$	1	int32
COT_patch	Mean and standard deviation of pixel values in patch	2	float32
CTP_patch	"	"	"
CER_patch	"	"	"
CPI_patch	Number of pixels in patch in {clear-sky, liquid, ice, undefined}	4	int32

Table 3: Information provided in AICCA for each $1^\circ \times 1^\circ$ grid cell: a cloud class label computed by RICC and a set of diagnostic quantities obtained by aggregating MODIS data over all patch pixels for that grid cell.

Variables	Description	Values	Type
Cell	(lat, long) for grid cell	2	float32
Timestamp	Time of observation	1	float32
Label	Most frequent class label in grid cell	1	int32
COT_1deg	Mean of pixel values in grid cell	1	float32
CTP_1deg	"	"	"
CER_1deg	"	"	"
CPI_1deg	Most frequent particle phase in grid cell	1	int32

Finally, we accumulate the aggregated grid-cell values to create the daily files. Given the MODIS orbital coverage, the complete OC-Gridcell set contains around $(20 + 22 \text{ years}) \times (365 \text{ days/year}) \times (65 \text{ 160 grid cells}) \times 32 \text{ B} \approx 29.8$ gigabytes.

3 Constructing AICCA

The AICCA production workflow, shown in Figure 1, consists of four principal stages: download, archive, and prepare MODIS satellite data; train the RICC unsupervised learning algorithm, and cluster cloud patterns and textures; evaluate the reasonableness of the resulting clusters and determine an optimal cluster number; and assign clusters produced by RICC to other MODIS data unseen during RICC training. We describe each stage in turn here. Both the RICC codebase and Jupyter notebook [Kluyver et al. \[2016\]](#) used in the analysis are available online [Kurihana \[2022\]](#), and the trained RI autoencoder used for this study is archived at the following link at the Data and Learning Hub for science (DLHub) [Chard et al. \[2019\]](#): <https://acdc.alcf.anl.gov/dlhub/?q=climate>. DLHub is a scalable and low-latency model repository to share and publish machine learning models to facilitate their reuse and reproduction.

3.1 Stage 1: Download, Archive, and Prepare MODIS Data

Download and archive. As noted in Section 2.1, we use subsets of the three MODIS products in this work, a total of 801 terabytes for 2000–2021. To employ high-performance computing resources at Argonne National Laboratory for AI model training and inference, all files are stored locally on an Argonne storage system. Transferring the files from NASA archives is rapid for the subset of the files accessible on a Globus endpoint at the NASA Center for Climate Simulation, which can be transferred via the automated Globus transfer system [Foster \[2011\]](#). The remaining files must be transferred from NASA LAADS via the more labor-intensive option of `wget` commands, which we accelerated by using the `funcX` [Chard et al. \[2020\]](#) distributed function-as-a-service platform to trigger concurrent downloads on multiple machines.

Prepare. The next step involves preparing the *patches* used for ML model training and inference. We extract from each swath multiple $128 \text{ pixel} \times 128 \text{ pixel}$ (roughly $100 \text{ km} \times 100 \text{ km}$) non-overlapping patches, for a total of ~ 331 million

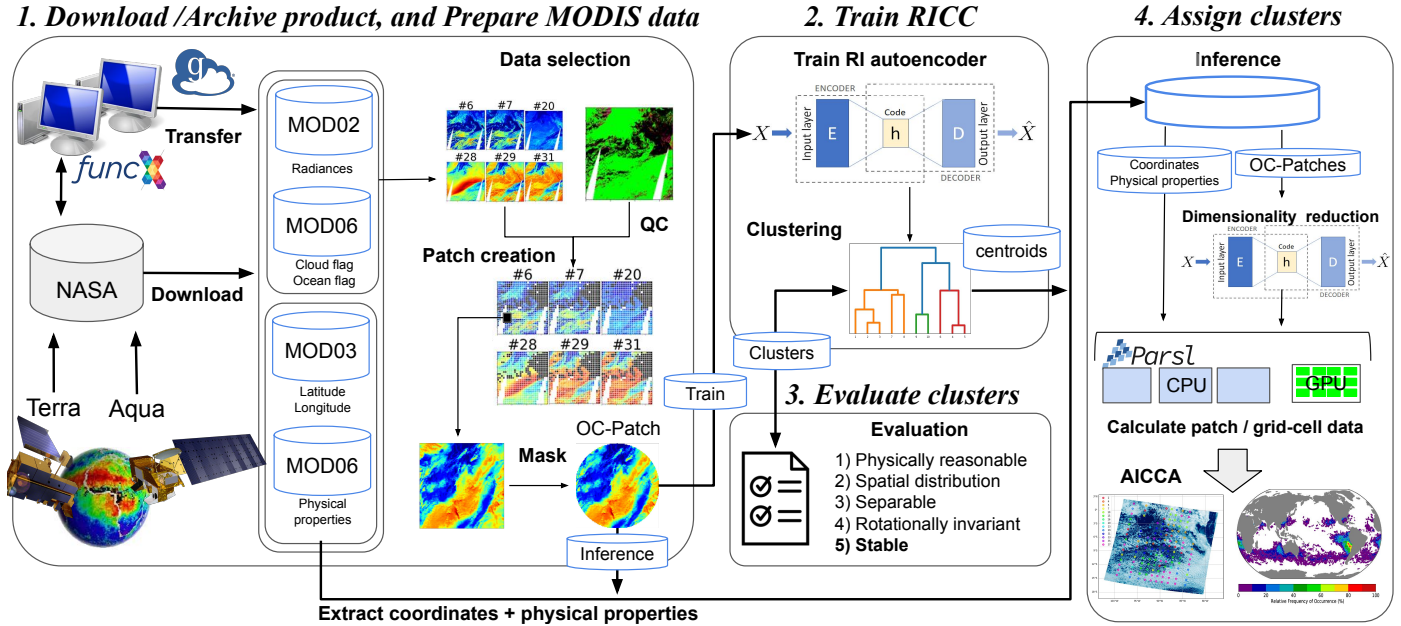


Figure 1: The AICCA production workflow comprises four principal stages. **1) Download/Archive and Prepare MODIS data:** Download calibrated and retrieved MODIS products from the NASA Level-1 and Atmosphere Archive and Distribution System (LAADS), using FuncX and Globus for rapid and reliable retrieval of 801 terabytes of three different MODIS products between 2000–2021. Store downloaded data on the Theta filesystem at the Argonne National Laboratory. Select six near-infrared to thermal bands related to clouds and subdivide each swath into non-overlapping 128×128 pixel patches by six bands. Select patches with $>30\%$ cloud pixels over ocean regions, and apply a circular mask for optimal training of our rotation-invariant autoencoder, yielding OC-Patches. **2) Train RICC:** Train an autoencoder to 1M randomly selected patches to generate latent representations, and cluster those latent representation to determine cluster centroids [Kurihana et al. \[2021\]](#). **3) Evaluate clusters:** Apply five protocols to evaluate whether the clusters produced are meaningful and useful. **4) Assign clusters:** Use trained autoencoder and centroids to assign cloud labels to unseen data. We use the Parsl parallel Python library to scale the inference process to hundreds of CPU nodes plus a single GPU, and to generate the AICCA dataset in NetCDF format. We then calculate physical properties and other metadata information for each patch and for each $1^\circ \times 1^\circ$ grid cell.

patches. We then eliminate those that include any non-ocean pixels as indicated by the MOD06 land/water indicator, since in these cases radiances depend in part on underlying topography and reflectance. (Note that even ocean-only pixels may involve surface-related artifacts in cases when the ocean is covered in sea ice.) We also eliminate those with less than 30% cloud pixels, as indicated by the MOD06 cloud mask. The result is a set of 198 676 800 *ocean-cloud patches*, which we refer to in the following as OC-Patches. (Note that the large number of cloud image patches mean that the RI autoencoder naturally has a degree of translation invariance, since because the translations of clouds relative to the patch boundaries are stochastic.) For each ocean-cloud patch, we take from the MOD02 product six bands (out of 36 total) for use in training and testing the rotation-invariant (RI) autoencoder, as well as the MOD04 and MOD06 data used for location and cluster evaluation as described in Section 2. For in-depth discussion of data selection, see [Kurihana et al. \[2021\]](#).

We also construct a training set $OC\text{-Patches}_{AE}$ by selecting a set of one million patches at random from OC-Patches. Because do not expect our RI autoencoder to be robust to the selection of MODIS data, we collect data from the entire 22-year period of MODIS operation at random. Using 1M patches ensures that they are not overly imbalanced among seasons or locations.

3.2 Stage 2: Train the RICC Autoencoder and Cluster Cloud Patterns

In this stage we first train the RI autoencoder and then define cloud categories by clustering the compact latent representations produced by the trained autoencoder.

Train RICC. The goal of training is to produce an RI autoencoder capable of generating latent representations (a lower-dimensional embedding as the intermediate layer of the autoencoder) that explicitly capture the variety of input

textures among ocean clouds and also map to differences in physical properties. We introduce general principles briefly here, but see our previous work [Kurihana et al. \[2021\]](#) for further details of the RI autoencoder architecture and training protocol.

An autoencoder [Hinton and Richard \[1994\]](#), [Hinton et al. \[2011\]](#) is a widely used unsupervised learning method that leverages dimensionality reduction as a preprocessing tool prior to image processing tasks such as clustering, regression, anomaly detection, and inpainting. The autoencoder consists of an encoder and decoder to learn both to encode the input images into a compact lower-dimensional latent representation and to decode that representation to output images. During training, a loss function minimizes the difference between input and output. The resulting latent representation in the trained autoencoder both 1) retains only relevant features for the target application in input images, and 2) maps images that are similar (from the perspective of the target application) to nearby locations in latent space.

The loss function minimizes the difference between an original and a restored image based on a distance metric during autoencoder training. The most commonly used metric is a simple ℓ^2 distance between the autoencoder’s input and output:

$$L(\theta) = \sum_{x \in S} \|x - D_{\theta}(E_{\theta}(x))\|_2^2, \quad (1)$$

where S is a set of training inputs; θ is the encoder and decoder parameters, for which values are to be set via training; and x and $D_{\theta}(E_{\theta}(x))$ are an input in S and its output (i.e., the restored version of x), respectively. However, optimizing with this common ℓ^2 loss function (Eq. 1) is inadequate for our purposes because it tends to generate different representations for an image x and a rotated image $R(x)$, as shown in Fig. 2, with the result that the two images end up in different clusters. Since any particular physically driven cloud pattern can occur in different orientations, we want an autoencoder that can assign cloud types to images regardless of orientation. Other ML techniques that combine dimensionality reduction with clustering algorithms have not addressed the issue of rotation-invariance within their training process. For example, non-negative matrix factorization (NMF) [Lee and Seung \[1999\]](#) can approximate input data into a low-dimensional matrix—i.e., produce a dimensionally reduced representation similar to an autoencoder—and can be used for clustering, but applications of NMF are not invariant to image orientation.

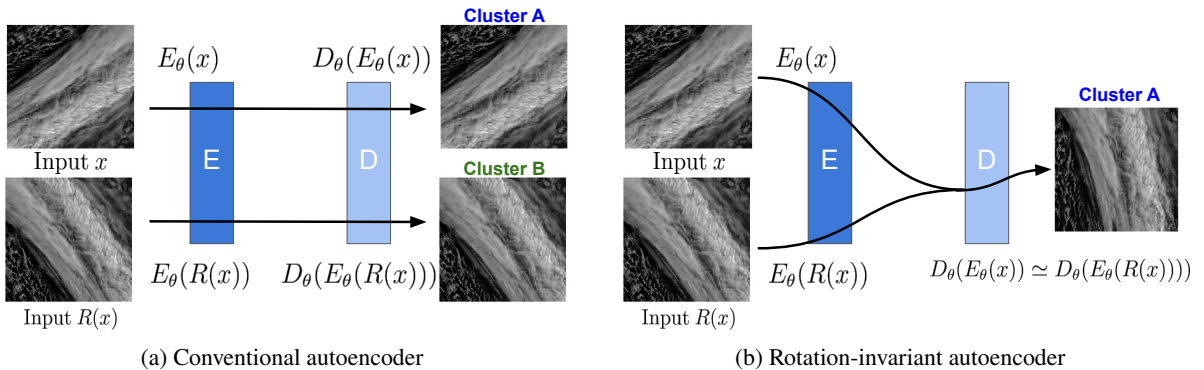


Figure 2: Illustration of the learning process when training (a) conventional autoencoder with Equation 1 vs. (b) rotation-invariant autoencoder with Equation 2. Because conventional autoencoder reflects orientation in the latent representation, two input images, which are identical texture but different orientation, are assigned to different clusters, A and B. However, rotation-invariant autoencoder produces latent representation that is agnostic to orientation. This allows clustering to place them both in the same cluster.

We have addressed this problem in prior work by defining a rotation-invariant loss function [Kurihana et al. \[2021\]](#) that generates a similar latent representations, agnostic to orientation, for similar morphological clouds and thus places those similar clouds in the same cluster (Fig. 2b). The RI autoencoder is motivated by a loss function used for the shifted transform invariant autoencoder of Matsuo et al. [Matsuo et al. \[2017\]](#). Our loss function L combines both a rotation-invariant loss, L_{inv} , to learn the rotation-invariance needed to map different orientations of identical input images into a uniform orientation, and a restoration loss, $L_{\text{res}}(\theta)$, to learn the spatial structure needed to restore structural patterns in inputs via autoencoder with high fidelity:

$$L = \lambda_{\text{inv}} L_{\text{inv}} + \lambda_{\text{res}} L_{\text{res}}, \quad (2)$$

where the scalars λ_{inv} and λ_{res} are the weights of the respective loss terms. The balance between the two parameters both achieve rotation-invariance and encodes spatial features:

$$L_{\text{inv}}(\theta) = \frac{1}{N} \sum_{x \in S} \sum_{R \in \mathcal{R}} \|D_{\theta}(E_{\theta}(x)) - D_{\theta}(E_{\theta}(R(x)))\|_2^2, \quad (3)$$

where \mathcal{R} is a set of rotation operators, each of which rotates an input by a different angle. To learn the spatial substructure in images, we compute the sum of minimum differences over the minibatch:

$$L_{\text{res}}(\theta) = \sum_{x \in S} \min_{R \in \mathcal{R}} \|R(x) - D_{\theta}(E_{\theta}(x))\|_2^2. \quad (4)$$

The L_{inv} computes, for each image in a minibatch, the difference between the restored original and all original rotations. Thus, minimizing Equation (3) produces similar latent representations for an image, regardless of its orientation, and so does the restored image because the optimization obtains values θ that preserve spatial structure in the input while enabling them to transform to a canonical orientation. For simplicity of optimization, we exclude a sparsity term used in Matsuo et al. [Matsuo et al. 2017], with the goal of minimizing the number of DNN nodes (“neurons”) required to achieve translation invariance in their latent representation.

Our RI autoencoder training protocol searches for the optimal combination of coefficients in the two loss terms and the best learning rate until the rotation-invariant loss converges to the training data. The optimal combination balances the transform-invariant and restoration loss terms. We determine $(\lambda_{\text{inv}}, \lambda_{\text{res}}) = (32, 80)$ as the optimal combination of the weights of the respective loss terms. The neural network architecture is the other factor needed to achieve rotation invariance: Following the heuristic approach of deep convolutional neural networks, our encoder stacks five blocks of convolutions, each with three convolutional layers activated by leaky ReLU [Nair and Hinton 2010], and with batch normalization [Ioffe and Szegedy 2015] applied at the final convolutional layer in each block before activation. We train our RI autoencoder on our one million training patches for 100 epochs by using stochastic gradient descent with a learning rate of 10^{-2} on 32 NVIDIA V100 GPUs in the Argonne National Laboratory ThetaGPU cluster.

Cluster Cloud Patterns. Once we have applied the trained autoencoder to a set of patches to obtain latent representations, we can then cluster those latent representations to identify the centroids that will define our cloud clusters. We use hierarchical agglomerative clustering (HAC) [Johnson 1967] for this purpose, and select Ward’s method [Ward Jr 1963] for the linkage metric, so that HAC minimizes the variance of square distances as it merges clusters from bottom to top. We have shown in previous work [Jenkins et al. 2019] that HAC clustering results outperform those obtained with other common clustering algorithms.

Given N data points, a naive HAC approach requires $O(N^2)$ memory to store the distance matrix used when calculating the linkage metric to construct the tree structure [Moertini et al. 2018]—which would be impractical for the one million patches in $\text{OC-Patches}_{\text{AE}}$. Thus, we use a smaller set of patches, $\text{OC-Patches}_{\text{HAC}}$, comprising 74 911 ocean-cloud patches from the year 2003 (the first year in which both Terra and Aqua satellites ran for the entire year concurrently) for the clustering phase. We apply our trained encoder to compute latent representations for each patch in $\text{OC-Patches}_{\text{HAC}}$ and then run HAC to group those latent representations into k^* clusters, in the process identifying k^* cluster centroids and assigning each patch in $\text{OC-Patches}_{\text{HAC}}$ a cluster label, $1..k^*$. The sequential scikit-learn [Varoquaux et al. 2015] implementation of HAC that we use in this work takes around 10 hours to cluster the 74 911 patches in $\text{OC-Patches}_{\text{HAC}}$ on a single core. While we could use a parallelizable HAC algorithm [Jin et al. 2015], [Sumengen et al. 2021], [Monath et al. 2021] to increase the quantity of data clustered, this would not address the intrinsic limitation of our clustering process given the 801 terabytes of MODIS data.

3.3 Stage 3: Evaluate Clusters Generated by RICC

A challenge when employing unsupervised learning is to determine how to evaluate results. While a supervised classification problem involves a perfect ground truth against which to output can be compared, an unsupervised learning system produces outputs whose utility must be more creatively evaluated. Therefore, we defined in previous work a series of evaluation protocols to determine whether the cloud classes derived from a set of cloud images are meaningful and useful [Kurihana et al. 2021]. We seek cloud clusters that: 1) are *physically reasonable* (i.e., embody scientifically relevant distinctions); 2) capture information on *spatial distributions*, such as textures, rather than only on mean properties; 3) are *separable* (i.e., are cohesive, and separated from other clusters, in latent space); 4) are *rotationally invariant* (i.e., insensitive to image orientation); and 5) are *stable* (i.e., produce similar or identical clusters when different subsets of the data are used). We summarize in Table 4 these criteria and the quantitative and qualitative tests that we have developed to validate them.

In our previous work [Kurihana et al. 2021], we showed that an analysis using RICC to separate cloud images into 12 clusters satisfies the first four of these criteria: it produces clusters that are not randomly distributed, do not contradict

Table 4: Our five-criteria evaluation protocol. We used the first four criteria in previous work [Kurihana et al. \[2021\]](#) to demonstrate that our quantitative and qualitative evaluation protocols can distinguish useful from non-useful autoencoders, even when common ML metrics such as ℓ^2 loss shows insignificant differences.

Criterion	Test	Requirement
Physically reasonable	Cloud physics	Non-random distribution; median inter-cluster correlation < 0.6
Spatial distribution	Spatial coherence	Spatially coherent clusters
	Smoothing	Low adjusted mutual information (AMI) score
	Scrambling	Low AMI score
Separable	Separable clusters	No crowding structure
Rotationally invariant	Multi-cluster	AMI score closer to 1.0
Stable	Significance of cluster stability	Ratio of Rand Index $G/R \geq 1.01$
	Similarity of clusterings	Higher Adjusted Rand Index (ARI)
	Similarity of intra-cluster textures	Lower weighted average mean square distance

existing physical knowledge, learn spatial information, are both cohesive in latent space and separated from each other, and are rotation-invariant. In this work we describe how we evaluate the last criterion, *stability*. Specifically, we evaluate the extent to which RICC clusters cloud textures and physical properties in a way that is stable against variations in the specific cloud patches considered, and that groups homogeneous textures within each cluster. We describe this process in Section 4 in the context of how we estimate the *optimal* number of clusters for this dataset associated with maximizing stability and similarity in clustering.

3.4 Stage 4: Assign Cluster Labels to Patches

We have so far trained our RI autoencoder on the 1 million patches in $\text{OC-Patches}_{\text{AE}}$ and applied HAC to the 74 911 patches in $\text{OC-Patches}_{\text{SHAC}}$ to obtain a set of k^* cluster centroids, $\mu = \{\mu_1, \dots, \mu_{k^*}\}$, where k^* is the number of clusters defined in Section 3.3. We next want to assign a cluster label to each of the 198 million patches in OC-Patches . We do this by identifying for each patch x_i the cluster centroid μ_k with the smallest Euclidean distance to its latent representation, $z(x_i)$. We use Euclidean distance as our metric because our HAC algorithm uses Ward’s method with Euclidean distance. That is, we calculate the cluster label assignment $c_{k,i}$ for the i -th patch as:

$$c_{k,i} = \arg \min_{k=\{1, \dots, k^*\}} \|z(x_i) - \mu_k\|_2. \quad (5)$$

This label prediction or *inference* process is easily parallelized. We use the Parsl parallel Python library [Babuji et al. \[2019\]](#), which enables scalable execution on many processors via simple Python decorators, for this purpose. We observe an execution time of 533 seconds per day of MODIS imagery (~13 000 patches) on 256 cores of the Argonne Theta supercomputer.

4 Evaluating Cluster Stability

Cluster stability is an important property for a cloud classification algorithm [Kurihana et al. \[2019\]](#). A clustering method is said to be *stable* for a dataset, D , and number of clusters, k , if it produces similar or identical clusters when applied to different subsets of D . As noted in Table 4, we define three tests to evaluate this criterion:

1. We measure *clustering similarity* by generating clusterings for different subsets of the same dataset, and calculating the average distance between those clusterings.
2. We measure *clustering similarity significance* by comparing each clustering similarity score to that obtained when our clustering method is applied to data from a uniform random distribution.
3. We measure *intra-cluster texture similarity* by calculating the average distance between latent representations in each cluster.

We are concerned not only to determine whether our clustering method, RICC, generates clusters that are stable, but also to identify the optimal number of clusters, k^* , to use for AICCA. In determining that number, we must consider all three tests just listed: we want a high clustering similarity, a high significance (certainly greater than 1), and a low intra-cluster similarity score.

For all of our stability tests, we work with $D = \{ \text{OC-Patches from 2003 to 2021, inclusive} \}$. $|D| \sim 180M$. (We do not consider data from 2000–2002 because Terra and Aqua were not operating at the same time for an entire year-long observation during that period.) We create a holdout subset H with number of patches $N_H = 14\,000$, and create $N = 30$ random subsets S_i with $N_R = 56\,000$ by sampling without replacement from $D \setminus H$. This procedure ensures the different S_i are mutually exclusive and there is no intersection between our holdout set H and the random subsets. The ratio $N_H : N_R$ of 20 : 80 is standard practice. We then create our 30 test datasets as $H \cup S_i$ for $\forall i \in \{1, \dots, 30\}$.

In the remainder of this section we describe three stability tests, whose results are shown in Figure 3. These tests lead us to choose 42 as the optimal number of clusters. We also conduct additional evaluations of whether the result of using RICC with 42 clusters creates cloud classes that have reasonable texture and physical properties, when compared to similar exercises with suboptimal numbers of clusters.

Algorithm 1 Pseudocode for the clustering similarity test described in Section 4.1.

Input: D : { OC-Patches for 2003–2021, inclusive }

Output: $G_8, \dots, G_{k_{\max}}$: Clustering similarity scores for cluster counts from 8 to k_{\max} .

```

1:  $H := \{x \mid x \in D\}$  where  $|H| = N_H$                                 ▶ Select holdout set to be used for evaluation
2: for  $i$  from 1 to  $N$  do
3:   Select a subset  $S_i := \{x \mid x \in D \setminus H \setminus \bigcup_{j=1}^{i-1} S_j\}$  with  $|S_i| = N_R$ 
4:   for  $k$  from 8 to  $k_{\max}$  do
5:      $\text{RICC}_k^i \leftarrow \text{Train RICC on } S_i \cup H$ 
6:      $C_k^i \leftarrow \text{RICC}_k^i(H)$                                        ▶ Determine cluster assignments in  $H$  with  $\text{RICC}_k^i$ 
7:   end for
8: end for
9: for  $k$  from 8 to  $k_{\max}$  do
10:   $G_k = \frac{1}{\binom{N}{2}} \sum_{(i,j) \in \binom{N}{2}} \text{ARI}(C_k^i, C_k^j)$                 ▶ Mean similarities for RICC clusters
11: end for
12: Return clustering similarity scores  $\{G_8, \dots, G_{k_{\max}}\}$ 

```

4.1 Stability Test 1: Clustering Similarity

We measure clustering similarity by first generating clusterings for different subsets of the target dataset and then calculating the average pairwise distance between those clusterings. We implement this approach as in Algorithm 1. As described above, we use as our dataset D all ocean-cloud patches from 2003–2021, inclusive; we define a holdout set, H , for evaluation (line 1); and we use as our “perturbed versions” N subsets selected without replacement from $D \setminus H$ (line 3). We then perform the following for different cluster numbers, i.e. For each k in the range $8 \leq k \leq k_{\max}$. We train RICC on each subset (line 8); we use the trained RICC to generate a clustering for the holdout set (line 6); we use the adjusted Rand index, ARI (see Appendix A) to evaluate pairwise distances between those clusterings (line 10); and we average among the 30 clusterings generated by the RICC models $\{\text{RICC}_k^i, i \in 1..30\}$ to determine the mean clustering similarity for that specific cluster number k . That is, we calculate the ARI for all $\binom{30}{2} = 435$ combinations of those 30 clusterings and determine the mean ARI score G .

The optimal number of clusters k^* should have $G > 0$, and a higher score indicates that patches are more stably grouped into the same clusters. Figure 3a shows that the mean ARI drops from 0.48 at eight clusters to 0.32 at 48 clusters, and then continues to decline to below 0.3 after 68 clusters. Although the ARI score of 0.32 with 48 clusters is far from the perfect score of 1, previous literature Santos and Embrechts [2009] on the relative association of ARI scores and supervised learning measures for multiclass datasets reports that an ARI of 0.29 corresponds to 58.55% in the classification correct percentage rate (COR) in the configuration of supervised learning, and that an ARI of 0.46 corresponds to 62.4% in COR. In addition, visual inspection suggests that the clusters produced by RICC stably group similar cloud patterns.

4.2 Stability Test 2: Significance of Similarities

Having determined how cluster similarity scores vary with number of clusters, we next turn to the question of whether these values are significant. Following Von Luxburg Von Luxburg [2010], we compare cluster similarity scores, as shown in Algorithm 2, against those obtained when the same method is applied to data generated not by our trained autoencoder but from a random uniform distribution (line 6) clustered with the same HAC method (line 11). We can

Algorithm 2 Pseudocode for the stability significance test described in Section 4.2.

Input: D : { OC-Patches for 2003–2021, inclusive }, trained rotation-invariant autoencoder AE

Output: $\{\frac{G_8}{R_8}, \dots, \frac{G_{k_{\max}}}{R_{k_{\max}}}\}$: cluster similarity significance scores

```

1:  $H := \{x \mid x \in D\}$  where  $|H| = N_H$  ▷ Select holdout set to be used for evaluation
2:  $z = \{AE(x) \mid x \in H\}$  ▷ Use trained autoencoder to compute latent representations
3:  $\sigma = \sqrt{\frac{1}{N_H} \sum_{j=1}^{N_H} (z_j - \bar{z})^2}$  ▷ Calculate standard deviation  $\sigma$  for latent representations
4: for  $i$  from 1 to  $N$  do
5:   Select a subset  $S_i := \{x \mid x \in D \setminus H \cup \bigcup_{j=1}^{i-1} S_j\}$  with  $|S_i| = N_R$ 
6:   Sample  $U_i := \{u \mid u \in \mathcal{U}[-2\sigma, 2\sigma]\}$  with  $|U_i| = N_H$ ,  $\mathcal{U}$  a random uniform distribution.
7:   for  $k$  from 8 to  $k_{\max}$  do
8:      $RICC_k^i \leftarrow$  Train RICC on  $S_i \cup H$ 
9:      $RICC_k^i(H) \leftarrow$  Determine cluster assignments in  $H$ 
10:     $HAC_k^i \leftarrow$  Train HAC on  $U_i$ 
11:     $HAC_k^i(U_i) \leftarrow$  Determine cluster assignments in  $U_i$ 
12:   end for
13: end for
14: ▷ Calculate averages of cluster similarities, as computed via Rand index,  $\text{RandI}(\cdot)$ , between all pairs of two label assignments resulting from RICC and a random distribution respectively
15: for  $k$  from 8 to  $k_{\max}$  do
16:    $G_k = \frac{1}{\binom{N}{2}} \sum_{(i,j) \in \binom{N}{2}} \left[ \text{RandI} \left( RICC_k^i(H), RICC_k^j(H) \right) \right]$  ▷ Mean similarities for RICC clusters
17:    $R_k = \frac{1}{\binom{N}{2}} \sum_{(i,j) \in \binom{N}{2}} \left[ \text{RandI} \left( HAC_k^i(U_i), HAC_k^j(U_j) \right) \right]$  ▷ Mean similarities for random clusters
18:   Calculate  $\frac{G_k}{R_k}$ , ratio of stability between RICC and random samples
19: end for
20: Return cluster similarities significance scores,  $\{\frac{G_8}{R_8}, \dots, \frac{G_{k_{\max}}}{R_{k_{\max}}}\}$ 

```

then compare how the ratio between those two values (line 18) varies with number of clusters. A ratio > 1 indicates that cluster assignments are more stably grouped than would be expected by chance; a value of 1 indicates that there are no benefit to adding extra clusters.

For each k in the range $8..k_{\max}$, we first compute clusterings as in the preceding clustering similarity test and then compute the mean clustering similarity score G , though here we use the Rand index (as described in Appendix A) rather than ARI, as we are not comparing scores across k . To produce random label assignments, we first prepare 30 datasets that are sampled from random uniform distributions $\mathcal{U} \in [-2\sigma, 2\sigma]$. We then apply HAC to the random data to generate random labels, from which we also calculate the Rand Index for 435 combinations, giving the mean score R . We expect the ratio of G/R to be higher than 1 if RICC cluster assignments are more stable than those obtained on the null reference distribution. We set a threshold of $G/R \geq 1.01$, meaning that the results obtained with RICC should be 1% or better than those with the null distribution. Figure 3b shows the significance of the stability values G/R as a function of the number of clusters k . The significance curve drops to 1.01 at 50 clusters, indicating that our optimal number of clusters is $k^* < 50$.

4.3 Stability Test 3: Intra-cluster Texture Similarity

A stable clustering should group patches with similar textures within the same cluster. To determine whether a clustering has this property, we examine how the average distance between latent representations within each cluster changes when we apply RICC to create different numbers of clusters. The mean distance between pairs of latent representations in a cluster relates to similarity of texture, as our RI autoencoder learns texture features and encodes those features in latent representations. Specifically, we calculate the mean squared Euclidean distance between the latent representations computed for patches in our holdout set H .

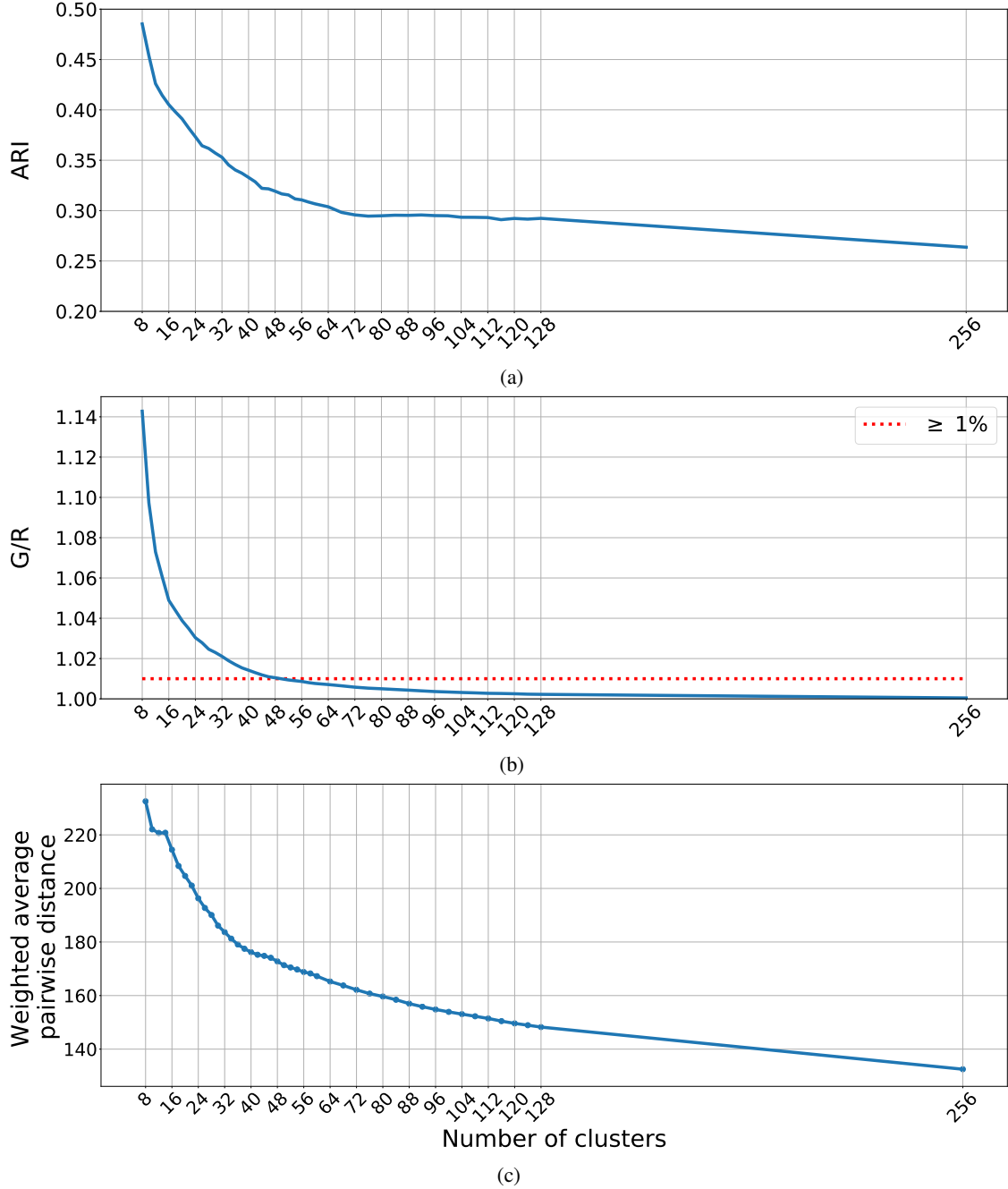


Figure 3: Plots for the three stability criteria metrics of Table 4, each as a function of number of clusters. (a) *Clustering similarity*: Adjusted Rand Index (ARI) as a measure of similarity of clusterings generated by RICC models trained on different subset of patches. (b) *Clustering similarity significance*: Blue line represents the ratio of the mean Rand Index based on RICC applied to our holdout patches $\{x \mid x \in H\}$ (G) and the mean Rand Index from HAC applied to random uniform distributions (R). The red dashed line is $G/R \geq 1.01$, indicating that the stability of cluster label assignments produced from RICC is $\geq 1\%$ better than results of simply clustering random uniform data. (c) *Intra-cluster texture similarity*: Blue line shows the weighted average of the mean squared Euclidean distance between pairs of patches within each cluster. Lower values suggest more homogeneous textures and physical features within each cluster. The use of three similarity tests enables to achieve simultaneously our goal of both stability and maximality when grouping clusters.

For a clustering with k clusters, let n_c be the number of elements in cluster c , and $y_1 \dots y_{n_c}$ be the patches in that cluster. As cluster sizes can vary, we weight each cluster’s mean distance by $w_c = n_c / \sum_{i=1}^k n_i$, to obtain a weighted average mean squared Euclidean distance:

$$d_k = \sum_{c=1}^k \left(w_c \sum_{i=1}^m \sum_{j>i}^m \frac{\|z(y_i) - z(y_j)\|_2^2}{\frac{m}{2}(m-1)} \right) \text{ where } m = \min(n_c, N_p), \quad (6)$$

where z represents the latent representations generated by our RI autoencoder, and N_p is the maximum number of patches to consider in the distance calculation—a limitation used to accelerate calculations. We set $N_p = 200$ for our tests. Note that when the total number of clusters is large, some individual clusters may have size less than this limit.

We calculate Equation 6 for k from 8 to 256 for each of our 30 clusterings of test subsets $\{\text{RICC}_k^1(H), \dots, \text{RICC}_k^{30}(H)\}$, and then compute the mean value across clusterings. The resultant weighted average distance decreases monotonically with the cluster number k (3c), as does the metric G/R from test 2, but the trends have opposite implications: lower values are worse in test 2 but better in test 3. A lower distance value indicates that cloud texture and physical properties are more homogeneous within a given cluster, meaning the resultant AICCA dataset provides a more consistent cloud diagnostic. The implication is that the optimal number of clusters k^* will be approximately the largest number that satisfies our criterion in test 2

In Figure 3c, the distance metric sharply decreases from 8 to 36 clusters, but the slope then flattens and values are almost unchanged between 40–48 clusters. That is, the pairwise similarity of latent representations drastically increases between 8 and 36 clusters but becomes less different among the range between 40–48 clusters. Selection of a k value from within this range would not change the result significantly. Since test 2 provides an upper bound of $k^* < 50$, the results of test 3 suggests the optimal number of cluster lies in $40 \leq k^* \leq 48$.

To summarize: We observe that as G/R decreases, ARI also declines, and that our G/R threshold requires $k^* < 50$. We observe that a cluster number in the range $40 \leq k \leq 48$ satisfies all three stability criteria. Note that we have validated that these choices also satisfy criteria 1–4 in Table 4.

4.4 Seasonal Variation of Textures within Clusters

The results of the three tests above indicate that choices in the range $40 \leq k^* \leq 48$ will yield clusters that not only are stably assigned but also group similar cloud texture patterns. We conduct one final check, investigating whether clusters produced via RICC show similar patterns regardless of season: we compare intra-cluster texture similarity between OC-Patches from January and July. if differences are small, the number of clusters used is sufficient to accommodate the large seasonal changes in cloud morphology.

We use RICC with the autoencoder trained on OC-Patches_{AE} and cluster centroids based on OC-Patches_{HAC}, for different numbers of clusters k , as before. For each k , we then apply the trained RICC_k model to the patches in OC-Patches_{HAC}: extract the latent representations for m_s randomly selected July patches and m_w randomly selected January patches in each of the resulting k clusters; and (as in Section 4.3) weight each cluster mean by January and July respectively. This weighting enables us to consider texture similarities from many clusters without results being dominated by trivial clusters that we observe to group fewer similar patches due to undersampling. We then sum the scores to obtain the overall weighted averaged squared distance (WASD) for k clusters. In summary:

$$\text{WASD} = \sum_{c=1}^k \left(w_c \sum_{i=1}^{m_s} \sum_{j=1}^{m_w} \frac{\|z(y_i^s) - z(y_j^w)\|_2^2}{m_s \cdot m_w} \right), \quad (7)$$

where n_c^s and n_c^w are the number of January and July patches in cluster c ; $y^s = y_1^s \dots y_{n_c^s}^s$ and $y^w = y_1^w \dots y_{n_c^w}^w$ are those patches; January We set $N_s = N_w = 100$ for this analysis.

We expand the analysis to account for two additional potential sources of bias. Because the specific days used in OC-Patches_{HAC} may affect our results, we assemble two different versions of OC-Patches_{HAC}, selecting two days without replacement from each season in 2003, as before. The resulting OC-Patches_{HAC-2} and OC-Patches_{HAC-3} have 77 235 and 76 143 patches, respectively. Similarly, to account for any effect of the random selection of the m_s summer and m_w winter patches, we repeat the analysis of Equation 7 three times for each of OC-Patches_{HAC}, OC-Patches_{HAC-2}, and OC-Patches_{HAC-3}. In this way we obtain a total of $9 \cdot k$ mean squared distance values and nine WASD values for each k in the range 8 to 256. These are shown as the dots in Figure 4. The WASD curve (black) decreases with increasing cluster number k , implying as expected that higher cluster numbers allow better capturing seasonal

changes. Because a smoothed version of the WASD curve (blue) has a minimum of $k=42$ over the range $40 \leq k \leq 48$, we choose 42 clusters as the optimum number and use this value in the inference step of Section 3.4.

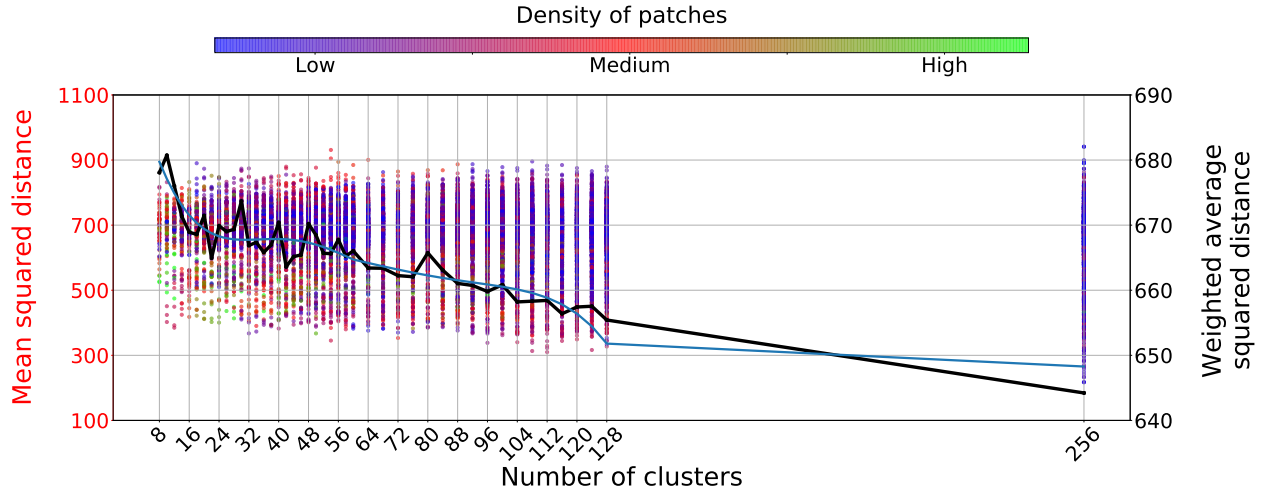


Figure 4: Seasonal stability test comparing the intra-seasonal variance of textures within each cluster as a function of number of clusters. Each of $9 \cdot k$ colored dots for each value of k gives the average squared distance (left y-axis) between July and January patches as described in text; the color indicates cluster density, a measure of cluster size. The black line shows the mean WASD (right y-axis) from nine trials, as described in the text. The blue line shows a smoothed WASD curve obtained by applying a Savitzky-Golay filter with degree six polynomial. The minimum WASD value occurs at $k = 42$ in the range of $40 \leq k^* \leq 48$, motivating our choice for AICCA.

4.5 Comparison of RICCs with Different Number of Clusters to ISCCP Classes

To investigate whether and how RICC clusters associate with the nine ISCCP cloud classes, we compare and contrast the frequencies of co-occurrence of (a) RICC clusters and (b) ISCCP classes. We evaluate how this relationship varies with cluster number used, considering not only the selected $k=42$ but also $k = 10, 64$, and 256.

Recall that each of the nine ISCCP classes is defined by a distinct range of cloud optical thickness (COT) and cloud top pressure (CTP) values [Rossow and Schiffer \[1999\]](#): high, medium, and low clouds, and thin, medium, and thick clouds. To compare RICC clusters with ISCCP classes, we calculate the relative frequency of occurrence (RFO) of RICC clusters across the same two-dimensional COT-CTP space, a standard approach to evaluating unsupervised learning algorithms [Tselioudis et al. \[2013\]](#), [McDonald and Parsons \[2018\]](#), [Schuddeboom et al. \[2018\]](#). For this evaluation, we use the cluster assignments obtained with RICC when trained on OC-Patches_{AE} and OC-Patches_{HAC} to produce the AICCA dataset, as described in Section 3. We take the Terra satellite ocean-cloud patches for January and July 2003, and for each cluster, use the mean and standard deviation of the COT and CTP values for its patches to define a rectangular region for that cluster within two-dimensional COT-CTP space that extends for one standard deviation on either side of the mean. We then calculate the number of clusters that are associated with each of the nine ISCCP classes by counting the number of clusters that overlap with that region of COT-CTP space and dividing this number by the total number of cluster-class overlaps for all clusters and classes. Note that the latter number will typically be greater than the number of clusters because a single cluster can extend over multiple ISCCP classes.

This analysis shows a similar proportionality between RICC unsupervised learning clusters and ISCCP observation-based classes. Table 5 compares the resulting proportions of RICC clusters (for each value of cluster number k) with the simple mapping of all patches to ISCCP classes based on their COT and CTP values (top line). In all cases, the Stratocumulus (Sc) class is the largest single category, and medium-thickness clouds (Sc, As, Cs) predominate at each altitude level. Stratocumulus (Sc) account for approximately 30% of RICC cluster overlaps, while the proportion of cloud observations in this category is over 50%. There is however no physical reason the numbers need be exactly the same: if for example all low medium clouds were identical in texture, we would expect they would be assigned to a single cluster. For all k values, relatively few RICC clusters are assigned to high clouds, as expected since these make up only $\sim 15\%$ of total cloud occurrences. The thin and medium ISCCP classes (Cu, Sc, Ac, As), which account for 78.4% of cloud occurrence in the MODIS dataset, are represented by a similar proportion of RICC cluster overlaps: 74.75%, 70.44%, and 71.40% for $k = 42, 64$, and 256 clusters, respectively. In general, the similarity of proportions suggest that AICCA is capturing physically meaningful distinctions between cloud types.

Table 5: ISCCP: Relative frequencies of occurrence based on mean COT and CTP values for OC-Patches from January and July, 2003. AICCA: Relative frequencies of occurrence of RICC clusters over each of the nine ISCCP cloud classes [Rossow and Schiffer \[1999\]](#), as determined by counting the number of clusters that overlap (as determined by the mean, plus or minus one standard deviation, of COT and CTP values for patches within each cluster) with each class, divided by the total number of cluster-class overlaps. We allow double counts if a cluster overlaps more than one ISCCP class. Results are given for $k=10, 42, 64,$ and 256 clusters, and for just January patches, just July patches, and both January and July patches. The AICCA values that are closest to the frequencies from MODIS column are in boldface. Recall that MODIS values are based on frequencies of *patches* over COT-CTP space, while the AICCA values are based on frequencies of *clusters* over COT-CTP space. Note that frequencies in each line add to 100, modulo rounding. We observe that the AICCA cluster frequencies are roughly proportional to the ISCCP category frequencies, although they constantly underestimate the Sc class (by 20%), and overestimate Cu and As classes.

Height			Low			Medium			High		
Thickness			Thin	Med	Thick	Thin	Med	Thick	Thin	Med	Thick
Dataset	Month	k	Cu	Sc	St	Ac	As	Ns	Ci	Cs	Dc
ISCCP	Jan & July 2003		5.29	53.94	2.93	3.65	15.50	2.12	3.39	10.52	2.60
AICCA $_k$	Jan 2003	10	11.42	25.71	8.57	5.71	22.85	8.57	2.85	8.57	5.71
		42	12.50	29.16	4.16	10.00	25.00	5.00	2.50	8.33	3.33
		64	10.38	34.41	3.24	7.79	26.62	3.24	0.64	9.74	3.89
		256	9.06	32.90	4.45	8.90	25.27	5.08	3.65	8.58	2.06
	July 2003	10	13.33	23.33	3.33	6.66	16.66	3.33	6.66	16.66	10.00
		42	10.30	30.92	4.12	7.21	20.61	4.12	3.09	13.40	6.18
		64	10.20	30.61	1.36	10.20	19.04	2.72	5.44	14.28	6.12
		256	9.31	32.16	2.46	8.78	21.61	1.93	5.97	13.53	4.21
	Jan & July 2003	10	12.50	25.00	6.25	3.12	18.75	3.12	9.37	15.62	6.25
		42	10.67	32.03	2.91	7.76	24.27	2.91	2.91	11.65	4.85
		64	8.80	29.55	3.77	8.17	23.89	5.03	5.03	11.94	3.77
		256	8.42	31.57	3.63	7.93	23.47	3.96	5.45	11.73	3.80

5 Results

Having determined an optimal number of clusters, k^* in Section 4, we then validate the scientific utility of AICCA $_{42}$ by evaluating the relationship between cloud class labels and their physical properties and spatial patterns. For this purpose we use labels for a dataset of 589 500 Terra ocean-cloud patches for January 2003 and July 2003.

5.1 Seasonal Variability of Cloud Cluster Regimes

Because the Earth is not symmetric, its clouds show strong seasonal variability not only in any given location but in the global mean. In this section we show that the physical properties of AICCA $_{42}$ clusters are reasonable and remain stable even if the dataset is restricted to a single month. This analysis builds on that from Section 4.4 and 4.5. In Section 4.4 we used intra-cluster seasonal differences as a criterion for choosing an optimal k of 42. In Section 4.5 we showed that RICC with $k = 42$ produced clusters whose proportions in COT-CTP space roughly matched the ISCCP classes of the patches used. We now plot the cluster distribution in COT-CTP space, and show that it is indeed reasonably constant across seasons (Figure 5).

As expected based on prior results, Figure 5 shows that most AICCA $_{42}$ clusters fall in the low cloud range (680–1100 hPa cloud top pressure) with low to medium optical thickness (2–20). (Compare to Table 5.) These results are broadly consistent with those of [Jin et al. \[2017\]](#), who performed a simple clustering analysis with the joint histogram of optical thickness and cloud top pressure, though Jin et al. [Jin et al. \[2017\]](#) obtained relatively more clusters associated with high clouds (four of their 11 clusters, vs. 5 of 42 in this work). The distribution of clusters is largely unchanged even when only January or July data are used in clustering. For example, the cumulus (Cu: left bottom) and stratocumulus (Sc: center bottom) regimes comprise 30 clusters in the full-year analysis, 30 in July only, and 32 in January only.

Using 42 clusters clearly allows RICC to capture richer cloud information than is in the limited set of 9 ISCCP cloud classes. In our previous work [Kurihana et al. \[2021\]](#), we found that 12 clusters were insufficient to achieve a clear separation between high and low clouds. In this work, the clusters from our cloud fields can distinguish the full range of physical properties here (from high to low CTP and thick to thin COT), though thin clouds are included only because

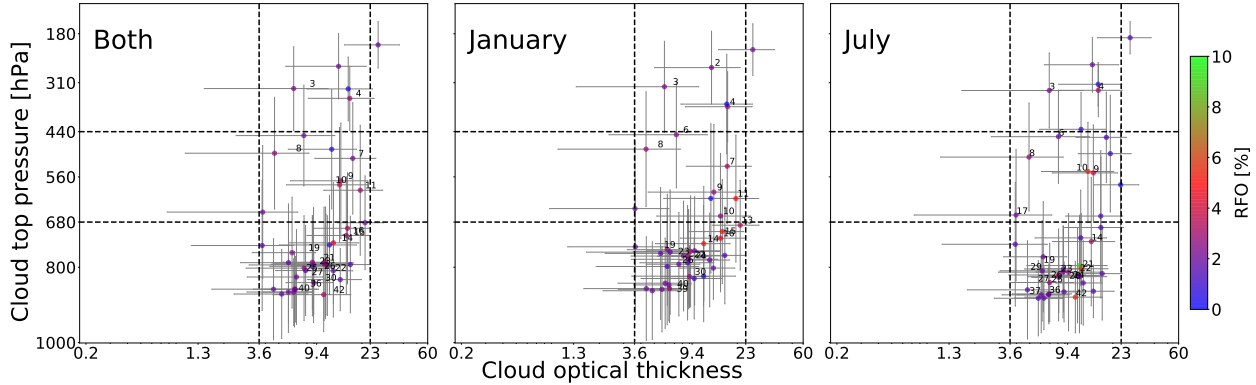


Figure 5: Distributions of cluster properties for AICCA₄₂ in cloud optical thickness (COT) – cloud top pressure (CTP) space, for January and July 2003 (left), January only (center), and July only (right). Dots show mean values for each cluster and error bars the standard deviation of cluster properties. Data point colors indicate the relative frequency of occurrence (RFO) of each individual cluster in the dataset. Note that in assigning cluster labels, we sort the clusters first on CTP and then on the global occurrence of the clusters within each 50 hPa pressure bin. Thus, small cluster numbers (e.g., #1) represent high-altitude cloud, and within a similar CTP range (e.g., 500 hPa – 550 hPa), smaller numbers represent the more dominant patterns within the bin. For clarity, we show only the 21 clusters with the highest RFOs. For comparison, dashed lines divide the COT-CTP space into the 9 regions corresponding to ISCCP cloud classes. AICCA₄₂ captures a greater variety of cloud types than do the ISCCP categories, with most of the clusters at low altitude (high CTP). Changes are small when analysis is repeated for a single month, indicating that AICCA₄₂ adequately captures seasonal variation in cloud properties.

our cloud clusters defined by means and error bars (i.e., standard deviation of the cloud parameter) cover more than one ISCCP class. The choice of a cluster number of 42 produces a reasonable trade-off.

5.2 Comparing AICCA₄₂ and ISCCP Classifications

We have previously verified that the cloud clusters produced by RICC are physically reasonable [Kurihana et al. \[2019\]](#). In Section 4.5 here, we also showed that RICC distributed those clusters in the COT-CTP space that defines established ISCCP classifications roughly in accordance with actual frequencies of cloud occurrence. In this section we investigate further how AICCA₄₂ clusters relate to these occurrence frequencies. The goal is to confirm that AICCA₄₂ diagnoses meaningful physical properties for use in climate science applications.

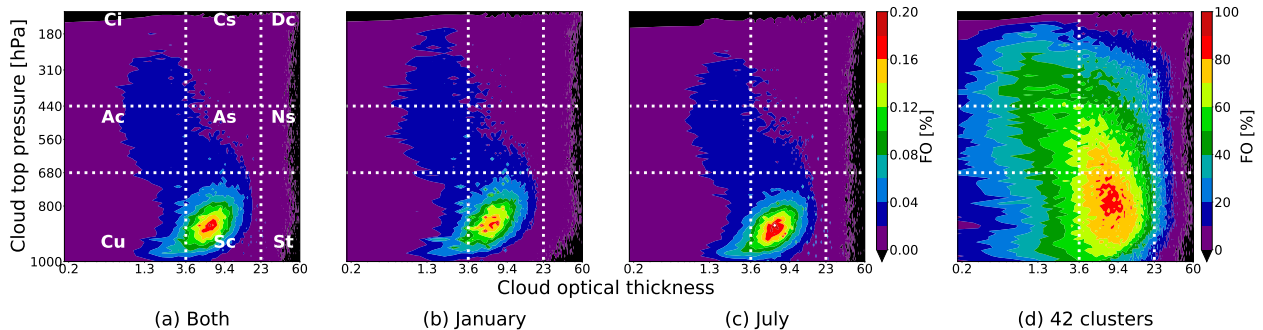


Figure 6: Comparison of a heatmap histograms for the frequency of occurrence (FO) on a two-dimensional joint cloud optical thickness (COT)–cloud top pressure (CTP) histogram (a–c) to cluster counts from AICCA₄₂ (d). Data used are all ocean-cloud patches from January and July 2003 from the Terra instrument. Panels (a)–(c) show the within-patch mean (μ_{COT} , μ_{CTP}) values from the MOD06 pixels, in bins of 0.5 in COT and 10 hPa in CTP. For the heatmap histogram of clusters (d), we count the number of clusters as described in text, at the same bin granularity. White dashed lines show boundaries of the nine ISCCP cloud classes [Rossow and Schiffer \[1999\]](#), clo: Cirrus (Ci), Cirrostratus (Cs), Deep convection (Dc), Altocumulus (Ac), Altostratus (As), Nimbostratus (Ns), Cumulus (Cu), Stratocumulus (Sc), and Stratus (St). AICCA₄₂ clusters cover all nine ISCCP classes, with the largest representation in the Stratocumulus (Sc) category where occurrence also peaks.

Figure 6 provides the fraction of all ocean-cloud patches from both January and July, January, July, and all clusters that overlap with a particular region of COT-CTP space; thus, for example, a heatmap value of 0.1% in a heatmap histogram of patches from both January and July indicates 5895 patches overlap with that histogram area, and in the 42 cluster case, a heatmap value of 50% indicates that 21 of 42 clusters overlap with that histogram area. We observe the highest degree of overlap with the Sc cloud class in all three heatmap histograms of patches, with 0.2% or more patches covering the area of around 860 hPa CTP and 3.6 to 9.4 COT. Clusters from AICCA₄₂ also tend to peak at Sc cloud class with 80 % or more clusters, but distribute more vertically between 700 to 900 hPa CTP. We also observe in Figure 6 that for no cluster count do we achieve more than 30% of overlap with the thick cloud class (St, Ns, Dc), and more than 60% of overlap with high altitude cloud class (Ci, Cs, Dc). Indeed, the comparison of cluster count to heatmap histograms of patches shows that the distribution of patches concentrates in Sc class (0–0.2%) than the other cloud classes (0–0.04%). The ratio of overlap suggests that our clusters partition cloud information more finely at low to middle cloud thicknesses and low cloud altitudes.

5.3 Separation of Ice and Liquid Phases

We showed in previous work (see Figure 10 in Kurihana et al. Kurihana et al. [2021]) that RICC-generated clusters differentiate between cloud that are dominated by ice vs. liquid phase. To refine the analysis of the association between the ratio of ice and liquid phases derived from cloud phased infrared (CPI) and other MOD06 cloud properties, we investigate the ratio of ice particles within clusters as a function of COT and CTP. Figure 7 shows the average percentage of ice particles in a patch. We see that clusters with low CTP (i.e., higher-altitude clouds) include a higher percentage of ice particles, which is consistent with physical interpretation, while clusters with high CTP include less than 20% ice particles. Furthermore, mid-altitude clouds (the middle row of Figure 7) combine ice and liquid phases, a result that is consistent with the transition of the particle phase from liquid to ice with altitude. This is reasonable to the cloud physics, and suggests that our clusters are influenced by cloud top pressure. But, distribution of ice particles are less distinct when comparing with the distribution of COTs. These results support the physical reasonableness of the AICCA dataset.

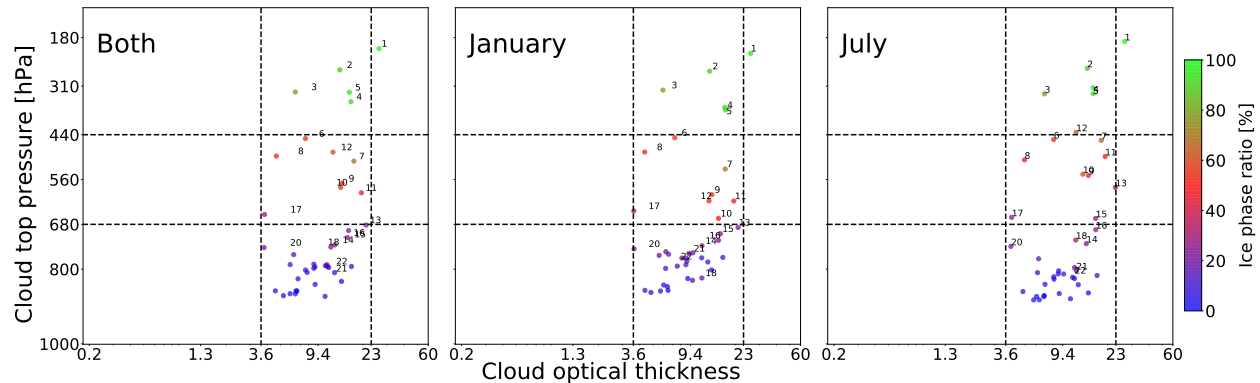


Figure 7: Can AICCA capture variations in cloud microphysics? We study here whether AICCA low- and high-altitude clusters have high liquid and ice fractions, respectively, as we would expect. The figure is constructed in the same way as Figure 5, but with each color marker showing the cluster’s *ice phase ratio*, defined as the mean within the cluster of the per-patch percentages of ice particle pixels: i.e., the percentage of the 128×128 pixels in the patch that have a CPI of “ice.” We associate number labels with clusters as in Figure 5, here for the 22 clusters with the highest ice phase ratios. We see that AICCA does indeed capture the diversity of cloud microphysics, with higher ice fractions in higher altitude clouds.

5.4 Case Study: Spatial Distribution of Cluster Labels Within a Swath

To examine whether our AICCA cloud classes exhibit unique geographical patterns and associations with known cloud objects, we examine the nature and distribution of AICCA cluster labels within two example MODIS swathes, as a case study. The example swathes, as shown in Figure 8a, are both off the coast of Peru: from Terra on January 15, 2003 (Figure 8b) and July 20, 2003 (Figure 8c). Each dot in Figures 8b and 8c denotes a cluster label assigned to a patch with >30% cloud pixels.

Visual inspection of the first swath, Figure 8b, reveals both open- and closed-cell stratocumulus clouds—and, right of center, from 80°W to 97°W, a transition from closed-cell to open-cell stratocumulus. The distinctive forms associated

with individual open-cell stratocumulus can be further subdivided, based on texture, as the open-cell structure becomes finer from 15°S to 0° . We also observe another texture characteristic of low clouds at the upper left scene of the swath, between 95°W and 103°W .

Visual inspection of the second swath, Figure 8c, reveals that open-cell stratocumulus clouds are dominant over most of the swath, from 72°W to 95°W , and surround closed-cell stratocumulus clouds, from 78°W to 87°W .

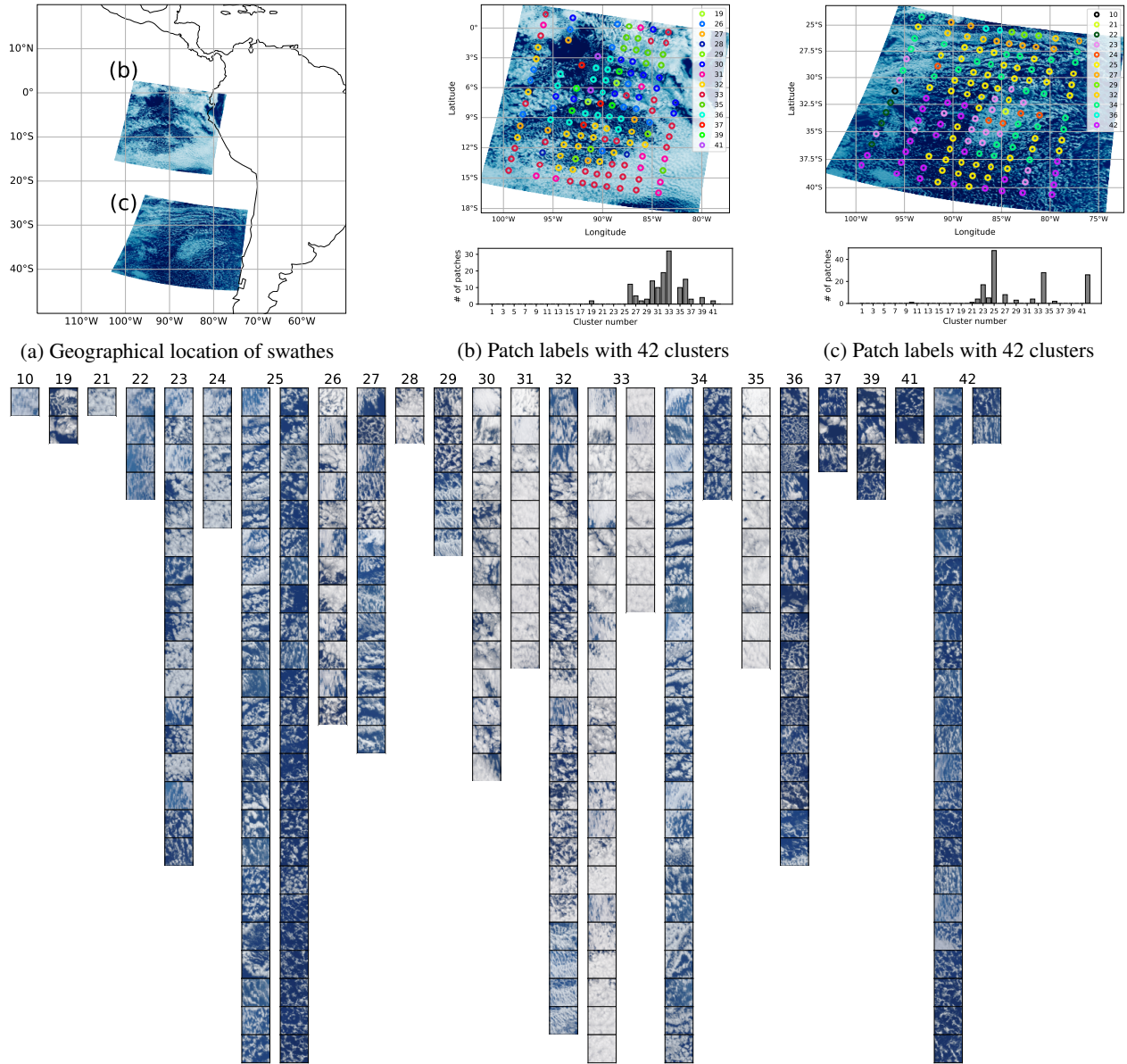


Figure 8: (a) The location of two swaths off the coast of Peru. (b) 133 ocean-cloud patches from the first swath (18°S to 3°N , 76°S to 104°S) observed by the Terra instrument on January 15, 2003. (c) 147 ocean-cloud patches from the second swath (44°S to 23°S , 72°S to 103°S) observed by the Terra instrument on July 20, 2003. In (b) and (c), each color marker denotes a patch cluster label, in the range 1..42 (not all clusters appear in each swath); the histograms show the distribution of cloud labels. (d) MODIS true color images [Gumley et al. \[2003\]](#) for the ocean-cloud patches from (b) and (c), grouped by cluster number. We see that AICCA produces spatially coherent cluster assignments for similar cloud objects: e.g., closed-cell stratocumulus in the lower part of (b) and (c). AICCA also captures richer information than the standard cloud classification, e.g., it separates the different textures of open- and closed-cell stratocumulus clouds into multiple classes.

Further visual inspection of both swathes shows both a pronounced *separation* among different cloud textures but also *coherence* when similar textures occur in neighboring pixels. In Figure 8b, #32 and #36 overlap the open-cell structure well, while #30, #31, #33, and #35 are widely stretched over the closed-cell stratocumulus clouds based on their morphological features. In Figure 8c, #25, #34, and #42 (not seen in Figure 8b) each cover open-cell stratocumulus clouds with different sparseness and texture characteristics. This spatial distribution of clusters suggests that, much as we saw when examining the appropriate numbers of clusters in Figure 5, the use of 42 clusters (rather than the nine cloud types in ISCCP) is beneficial in that it allows AICCA to represent intermediate cloud patterns and thus to classify marginal patches, such as those at margins between clouds, into additional cloud classes. However, we note that when in a separate experiment we labeled the swath of in Figure 8b with RICC_{256} (not shown in this article), we found 46 clusters were used to capture 133 patches, suggesting that too many clusters may harm understanding of cloud patterns by excessive differentiation of fine detail.

5.5 Use Case: Spatial Distribution of Aggregated Cluster Labels and Physical Properties

In this final study we examine the geographic distribution of, and association of the COT and CTP cloud parameters with, different AICCA cluster labels. We leverage the AICCA grid cell dataset to generate, as shown in Figure 9 42 plots, one per label, of the label’s RFO during January and July, 2003, for each 1° grid cell on a global grid. This application provides a good case study of how AICCA can, by providing data on a familiar latitude-longitude coordinate system, facilitate climate researcher understanding of spatial-temporal cloud patterns and regimes.

Reviewing Figure 9, we note first that various of the subfigures display spatial distributions that are associated with patterns of known cloud classes. For example, clusters #1–#3 appear in the tropical West Pacific, with different COTs: #1 shows a relatively thicker mean COT 23.9, at high-altitude 231.9 hPa on average, indicating good association with typical convective tropical clouds formed by warmer sea surface temperatures. In contrast, the thinner (COT 6.1) cloud cluster #3 appears to be capturing outflow cirrus clouds associated with deep convective activities in the tropical ocean.

We also observe spatial and physical associations with marine stratocumulus (Sc) clouds. We find, based on qualitative evaluation, that #30, #33, and #35 overlay closed-cell Sc clouds, while #25, #32, and #36 correspond to open-cell Sc clouds, with the former occurring along the west coast of continents (e.g., North / South East Pacific, South East Africa, and Southeast Indian Ocean) and the latter are surrounded by closed-cell Sc clouds and are found primarily in mid latitudes. All six of the clusters just listed have a mean CTP of 803–901 hPa, which corresponds to the typical cloud height of the Sc class. Differences between clusters with open and closed-cell structures associate with cloud optical thickness, with #33 and #35 showing clear closed-cell textures and thicker COT values (in the range 11.9–13.6), whereas clusters with open-cell structure (#25, #32, and #36) show relatively thinner COT values (5.7–7.1). The different mean optical thicknesses seen in our clusters match those of a previous classification study [Yuan et al. \[2020\]](#) that used 1000 scenes, each of 128×128 pixels, of MODIS data from the Aqua instrument from 2006 in the southeastern Pacific region—a correspondence that verifies the usefulness of our cloud clusters. The results also suggest that our aggregation output still captures various features resulting from the RICC system, even after the aggregation process. We conclude that (1) our methodology has explanatory power, in that it captures regionally unique cloud classes, and (2) 42 clusters is a useful number for a global analysis.

Zooming in on the six clusters just noted, we show in Figure 10 true color images [Gumley et al. \[2003\]](#) for the 20 patches closest to the $\text{OC-Patches}_{\text{HAC}}$ centroid for each of the six clusters. We observe that the patches shown for each cluster have similar textures, while patches from different clusters display distinct differences in cloud pixel density and in their open-cell/closed-cell/disorganized structure—evidence that AICCA_{42} is separating different stratocumulus clouds in terms of texture.

6 Discussion

Here, we discuss the stability protocol results presented in Section 4, potential contributions of AICCA, and directions for future work.

6.1 Stability Protocol

We have used the stability protocol described in Section 4 to determine a suitable number of clusters, given our twin goals of achieving a stable grouping of patches and maximizing the richness of the information contained in our clusters. Recall that Von Luxburg’s normalized stability protocol [Von Luxburg \[2010\]](#) simply minimizes an instability metric to determine the number of clusters that maximizes stability. In contrast, we combine three tests—adjusted cluster similarity, normalized stability, and weighted intra-cluster distance—to address the stability criterion. We use these

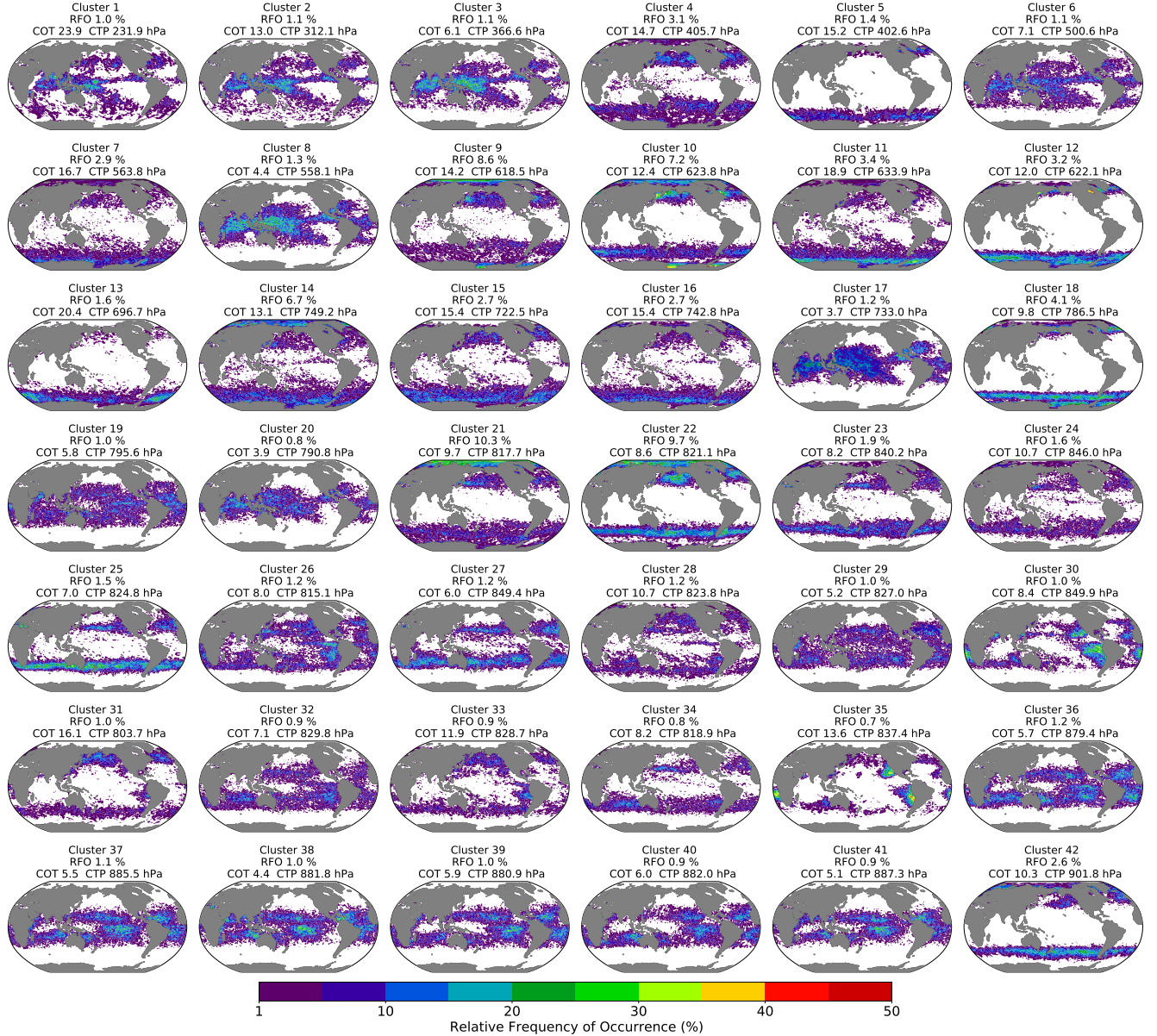


Figure 9: An example application of AICCA. We plot the relative frequency of occurrence (RFO) in January and July, 2003, for each of the 42 AICCA₄₂ clusters. Land is in grey, and areas where RFO < 1.0% are in white. Surtitles shows global mean RFO, cloud optical thickness (COT), and cloud top pressure (CTP) for the given cluster. We observe that clusters with roughly similar spatial patterns have slightly different global mean COTs, CTPs, and RFO distributions, suggesting meaningful physical distinctions.

tests to evaluate whether the cloud clusters produced by our unsupervised learning approach can provide meaningful insights for climate science applications.

This use of multiple similarity tests is essential to achieving our goal of both stability and maximality when grouping clusters. The *clustering similarity* test gives a mean score of scaled values calculated by ARI as a measurement of the degree of stability in OC-Patches. While this value is easy to understand when the resulting mean ARI is close to 1 (i.e., OC-Patches are always clustered into the same cluster group), ARI when applied to real world data could result in a value that is close to neither 0 nor 1 Santos and Embrechts [2009].

The *significance of similarities* test enables us to find the number of clusters after which there is reduced merit, from the perspective of stability against the null reference distribution, in adding more clusters. Normalized stability thus

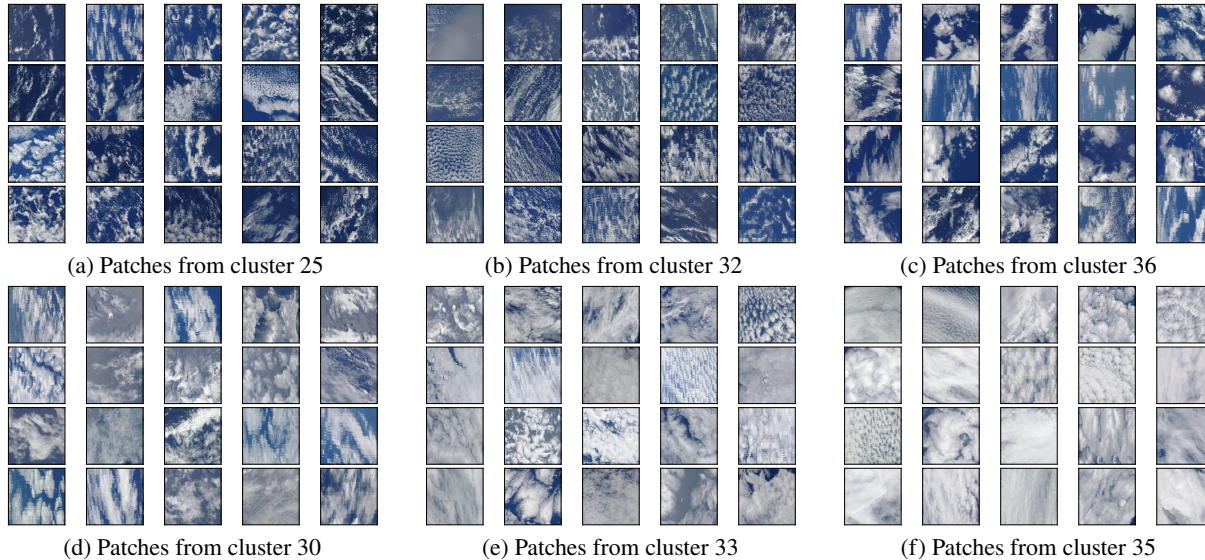


Figure 10: MODIS true color images [Gumley et al. \[2003\]](#) for the 20 patches closest to $OC\text{-}Patches_{HAC}$ centroids for six clusters that were seen in Figure 9 to feature typical open-cell stratocumulus clouds (upper row) and closed-cell stratocumulus clouds (lower row). White-to-gray colors indicate cloud pixels, and blue color represents ocean pixels. These selected six clusters distribute over typical regions of persistent low altitude clouds in Figure 9. We observe that: the open-cell clouds of #25 show larger empty cell structures than those of #32; #36 shows a sparse group of larger individual clouds; both #33 and #35 capture closed-cell stratocumulus clouds well, but #35 groups optically thicker clouds than those seen in #35; and #30 puts closed-cell and disorganized stratocumulus clouds together in terms of their textures.

provides statistical support for eliminating certain cluster numbers, especially when the first test produces an ARI value that is close to neither 0 nor 1.

We introduce the *similarity of intra-cluster textures* test because common approaches to estimating an optimal number of clusters, such as the elbow method [Bholowalia and Kumar \[2014\]](#), silhouette method [Rousseeuw \[1987\]](#), and gap statistics [Tibshirani et al. \[2001\]](#), seek to determine the *minimum* number of clusters needed to characterize a dataset—but in our application, achieving a minimum number of clusters might result in the merging of sub-clusters that in fact have unique textures and slightly different physical properties. By minimizing the intra-cluster difference shown in Figure 3c until the slope of the curve of distance becomes small, the third test causes the lower bound on the optimal number of clusters to increase to $40 \leq k^*$, avoiding oversimplifications.

A disadvantage of our stability protocol is that, unlike other heuristic approaches [Tibshirani et al. \[2001\]](#), [Von Luxburg \[2010\]](#), it does not always determine an unique optimal number of clusters. Indeed, our stability protocol in Section 4 concludes that $40 \leq k^* \leq 48$. Determining a single optimal number in the range sandwiched by the results of the three tests ultimately requires a subjective choice, based for example on the structure of cloud clusters in $OC\text{-}Patches_{HAC}$. In this study, we chose 42 as the number in the range $40 \leq k^* \leq 48$ that minimizes the seasonal variation of textures within clusters: see Section 4.4—although we note that a different selection of $OC\text{-}Patches$ in $OC\text{-}Patches_{HAC}$ could motivate a different value.

6.2 Future Perspectives for AICCA

Given the importance of clouds in projections of climate change, there is growing interest in the climate science community in methods that can exploit the underutilized information in decades (and petabytes) of satellite observations. Few large-scale satellite studies of cloud properties have previously been conducted [Zhao et al. \[2016\]](#), and automated cloud classification is critical to facilitate studies of the physical factors that govern spatial cloud patterns and their temporal changes.

In training RICC, we made use of neither physical properties nor spatial information. Yet our evaluations show that RICC clusters have mean cloud properties that are significantly associated with cloud physics. These results encourage us to extend our investigation to study 22-year global trends in the distribution and transition of cloud patterns with the AICCA dataset. We anticipate that the AICCA dataset will help shed light on changes on multiple timescales, from the

internal dynamics of weather systems, to natural or seasonal variability in the Earth’s atmosphere, to long-term forced anthropogenic climate change.

AICCA also opens up new possibilities for the evaluation and improvement of climate models. As climate simulations begin to be run at scales fine enough to resolve complex cloud textures Norman et al. [2022], the community needs methods to evaluate their ability to correctly capture those patterns and textures. Model intercomparison exercises (e.g., the High Resolution Model Intercomparison Project: HighResMIP Haarsma et al. [2016]) have not yet directly targeted cloud patterns due to the lack of a well-defined metric. The generation of a set of cloud classes via data-driven algorithms will allow for comparing models both with each other and with observations: either by comparing frequencies of common set of cloud classes, or by comparing the properties of classes that emerge from clustering each models output separately. ML approaches for cloud classification can also help in interpreting future climate models projections. For example, an open question in climate science is the likelihood of a catastrophic breakup of stratocumulus decks under extreme warming, which has been seen in some studies Schneider et al. [2019]. The application of our RICC algorithm to climate model outputs can help in evaluating the plausibility of this breakup.

6.3 Availability of Data and Code

The public availability of the complete AICCA dataset covering the 22-year period 2000–2021 will enable investigations of multidecadal global trends in the distribution of cloud patterns, frequencies, and behaviors. To further enhance the findability, accessibility, interoperability, and reusability (FAIRness) Wilkinson et al. [2016] of both the AICCA dataset and the code used to generate it, we are also working to capture and share our full end-to-end unsupervised learning workflow to enable its use for other cloud research projects Madduri et al. [2019], Chard et al. [2016]. Important components will include the provision of Python packages and APIs for AICCA download, versioning of AICCA (i.e., by varying the selection of the data used for training RICC and the reference centroids used to assign clusters), and the publication of models and datasets in easily reused forms. All AICCA datasets will be described with suitable metadata, referenced with long-lived identifiers (DOIs), and made accessible on high-speed storage at the University of Chicago’s Research Computing Center and the Argonne Leadership Computing Facility.

7 Conclusion

In this work, we have introduced an AI-driven cloud classification atlas that demonstrates the first global-scale unsupervised cloud classification of MODIS satellite imagery. We also described the protocol that we use to determine the optimal number of clusters for characterizing our MODIS ocean cloud data. We leverage common data formats (NetCDF) and data manipulation tools to make the AICCA₄₂ dataset and model repository accessible and reusable.

We address the stability criteria of five proposed five evaluation protocols (physically reasonable, spatial distributions, separable, rationally invariant, and stale) that asks whether derived cloud clusters from RICC are meaningful and useful for the climate application due to the insufficient definition of existing cloud classification. With the resultant optimal number of clusters $40 \leq k^* \leq 48$ based on our stability protocol, we apply RICC to global ocean cloud patches for months January and July in the year 2003, sub-sampled from the AICCA₄₂ dataset. These results show that our clusters in AICCA₄₂ are able to represent richer cloud information than the standard cloud classification. The groupings into clusters are reasonable in terms of mean physical properties, and also incorporate information about cloud textures. The geographic distribution of cloud types appears physically reasonable and offer the possibility of immediate use in atmospheric science. In particular, the richer classification of stratocumulus clouds, one of the major uncertainties in global warming projections, should open up new possibilities for studying their evolution in existing observational datasets. More broadly, unsupervised learning algorithms offer the possibility of unlocking large satellite datasets and making them tractable for analysis. This documentation is intended to facilitate the extension of RICC to new problems by researchers in other fields.

The AICCA dataset is publicly available at: <https://github.com/RDCEP/clouds#download-aicca-dataset> (accessed on 26 August 2022). The rotation-invariant autoencoder can be found at: <https://acdc.alcf.anl.gov/dlhub/?q=climate>. Our codebases and Jupyter notebooks are available in Github: <https://github.com/RDCEP/clouds>

Acknowledgement

The authors thank Rebecca Willett and Davis Gilton for contributing to the RICC design; Scott Sinno for providing MODIS products from the NASA Center for Climate Simulation; NASA for access to MODIS data; Zhuozhao Li, Sandro Fiore, and Donatello Elia for collaboration and feedback on the AICCA workflow; and the Argonne Leadership

Computing Facility and University of Chicago’s Research Computing Center for access to computing resources. We also thank to James Franke and Ziwei Wang to create AICCA dataset and conduct analysis shown in Appendix section.

Appendix A Rand Index and Adjusted Version for Chance

We describe the Rand index used in Section 4. Let $U = \{U_1, \dots, U_r\}$ and $V = \{V_1, \dots, V_c\}$ be two clustering partitions of a set of N objects $O = \{o_1, \dots, o_{N_p}\}$, such that $\bigcup_{i=1}^r U_i = \bigcup_{j=1}^c V_j = O$, and $U_i \cap U_{i'} = \emptyset$ as well as $V_j \cap V_{j'} = \emptyset$ for $1 \leq i \leq r$ and $1 \leq j \leq c$. We count how many of the $\binom{N}{2}$ possible pairings of elements in O are in the same or different clusters in U and V :

- P_{11} : number of element pairs that are in the *same* clusters in both U and V
- P_{10} : number of element pairs that are in *different* clusters in U , but in the *same* cluster in V
- P_{01} : number of element pairs that are in the *same* cluster in U , but in *different* clusters in V ; and
- P_{00} : number of element pairs that are in *different* clusters in both U and V .

The Rand index then computes the fraction of correct cluster assignments:

$$\text{RandI}(U, V) = \frac{P_{11} + P_{00}}{P_{11} + P_{10} + P_{01} + P_{00}} = \frac{P_{11} + P_{00}}{\binom{N}{2}} \quad (8)$$

It has value 1 if all pairs of labels are grouped correctly and 0 if none are correct. The metric is independent of the absolute values of the labels: that is, it allows for permutations.

To illustrate how the Rand index works, consider the two clusterings: $A = \{d_1\}, \{d_2, d_3\}$ and $B = \{d_1, d_2\}, \{d_3\}$ of the dataset $D = \{d_1, d_2, d_3\}$. Here, $N = 3$, and there are $\binom{3}{2} = 3$ possible pairings of the three dataset elements: $(d_1, d_2), (d_1, d_3), (d_2, d_3)$. Thus: $P_{11} = 0$, as no pair is in the same cluster in both A and B ; $P_{10} = 1$, as d_1 and d_2 are in different clusters in A but the same cluster in B ; $P_{01} = 1$, as d_2 and d_3 are in different clusters in A but the same cluster in B ; and $P_{00} = 1$, as d_1 and d_3 are in different clusters in both A and B . Hence, the Rand index by Equation 8 of A and B is $(0 + 1)/3 = 0.33$.

A difficulty with the Rand index is that its value tends to increase with the number of clusters, hindering comparisons across different numbers of clusters. In order to permit comparisons of Rand index values across different numbers of clusters, the **adjusted Rand index** (ARI) [Hubert and Arabie \[1985\]](#) corrects for co-occurrences due to chance:

$$\text{ARI}(U, V) = \frac{\binom{N}{2} (P_{11} + P_{00}) - [(P_{11} + P_{10})(P_{11} + P_{01}) + (P_{01} + P_{00})(P_{10} + P_{00})]}{\binom{N}{2}^2 - [(P_{11} + P_{10})(P_{11} + P_{01}) + (P_{01} + P_{00})(P_{10} + P_{00})]}, \quad (9)$$

where the P_{xy} are as defined above.

Appendix B Mean Patch Occurrence and Trends

For summary, we show mean patch occurrence across all 42 classes as well as optical thickness from the mean MODIS properties for reference in Figure 11. Linear trends are calculated at the yearly aggregate labels from 2003–2020 in each 1 degree spatial bin.

While not all locations have significant strong trends, we observe that cloudy places are getting more cloudy. Mean COT and results from trend analysis in Figure 11 explain that clouds with larger COT have a positive trend and low COT have negative trend. Especially, COT and their trends at bottom row in Figure 11 tell that under cloudy condition thicker clouds get thicker between 2003–2021.

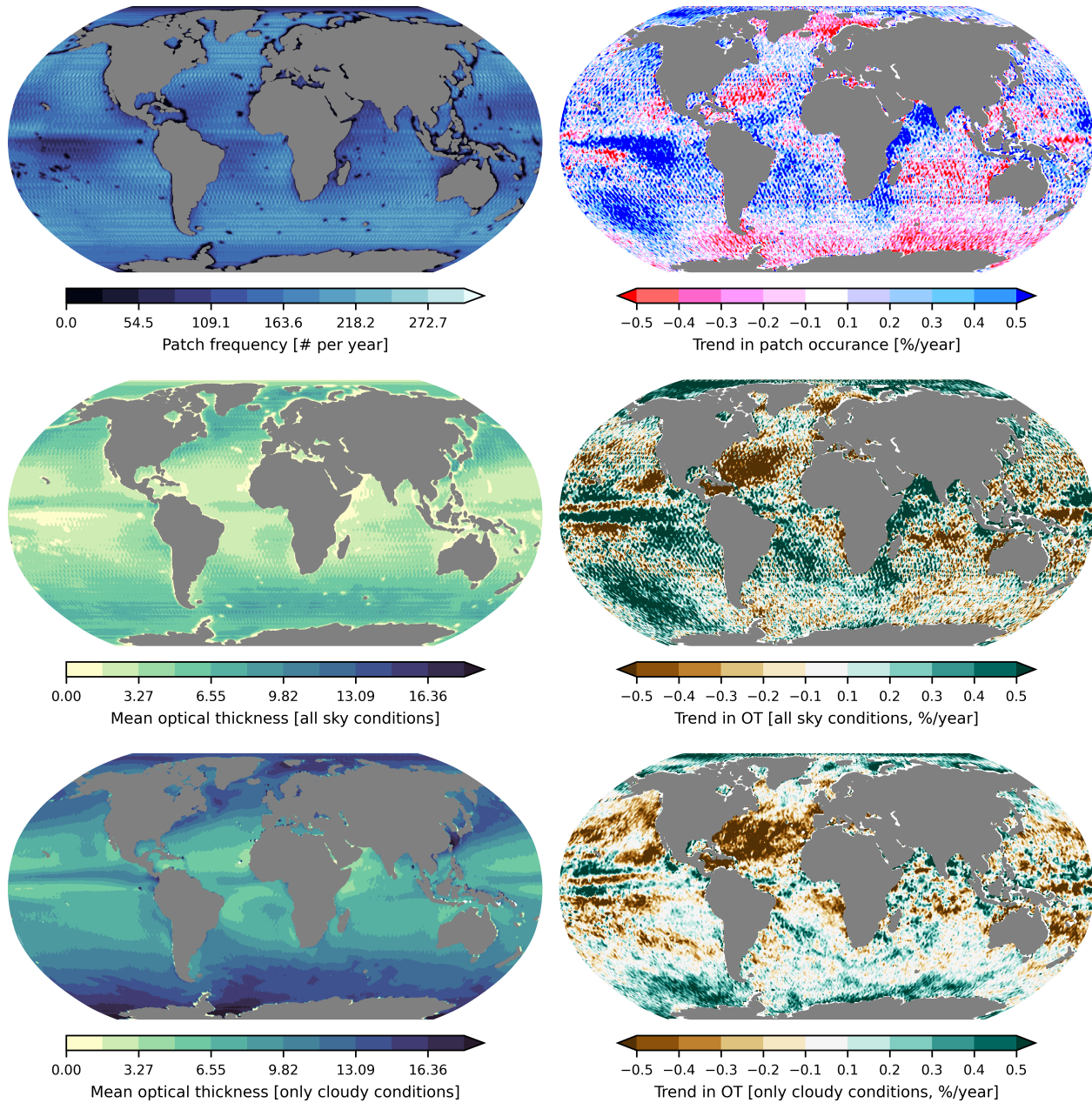


Figure 11: Left column: mean patch occurrence (across all 42 class labels), mean optical thickness in all sky conditions, and mean optical thickness only when identified cloud patches are present. Right column: linear trends in these values shown as a percent change per year compared to the mean value in each grid cell across all years. Data from 2003-2021.

References

- ISCCP Definition of Cloud Types. <https://isccp.giss.nasa.gov/cloudtypes.html>. Visited May 1, 2022.
- Yadu Babuji, Anna Woodard, Zhuozhao Li, Daniel S Katz, Ben Clifford, Rohan Kumar, Lukasz Lacinski, Ryan Chard, Justin M Wozniak, Ian Foster, et al. Parsl: Pervasive parallel programming in Python. In *28th International Symposium on High-Performance Parallel and Distributed Computing*, pages 25–36. IEEE, 2019.
- Purnima Bholowalia and Arvind Kumar. Ebc-means: A clustering technique based on elbow method and k-means in wsn. *International Journal of Computer Applications*, 105(9), 2014.
- Kyle Chard, Mike D’Arcy, Ben Heavner, Ian Foster, Carl Kesselman, Ravi Madduri, Alexis Rodriguez, Stian Soiland-Reyes, Carole Goble, Kristi Clark, et al. I’ll take that to go: Big data bags and minimal identifiers for exchange of large, complex datasets. In *IEEE International Conference on Big Data*, pages 319–328. IEEE, 2016. doi: 10.1109/BigData.2016.7840618.
- Ryan Chard, Zhuozhao Li, Kyle Chard, Logan Ward, Yadu Babuji, Anna Woodard, Steven Tuecke, Ben Blaiszik, Michael J. Franklin, and Ian Foster. DHub: Model and data serving for science. In *IEEE International Parallel and Distributed Processing Symposium*, pages 283–292, 2019. doi: 10.1109/IPDPS.2019.00038.
- Ryan Chard, Yadu Babuji, Zhuozhao Li, Tyler Skluzacek, Anna Woodard, Ben Blaiszik, Ian Foster, and Kyle Chard. FuncX: A federated function serving fabric for science. In *29th International Symposium on High-performance Parallel and Distributed Computing*, pages 65–76, 2020.
- L. Denby. Discovering the importance of mesoscale cloud organization through unsupervised classification. *Geophysical Research Letters*, 47(1):e2019GL085190, 2020. doi: 10.1029/2019GL085190.
- Ian Foster. Globus online: Accelerating and democratizing science through cloud-based services. *IEEE Internet Computing*, 15(3):70–73, 2011. doi: 10.1109/MIC.2011.64.
- Liam Gumley, Jacques Descloitres, and Jeffrey Schmaltz. Creating reprojected true color modis images: A tutorial. *University of Wisconsin–Madison*, 19, 2003.
- Reindert J Haarsma, Malcolm J Roberts, Pier Luigi Vidale, Catherine A Senior, Alessio Bellucci, Qing Bao, Ping Chang, Susanna Corti, Neven S Fućkar, Virginie Guemas, et al. High resolution model intercomparison project (highresmpip v1. 0) for cmip6. *Geoscientific Model Development*, 9(11):4185–4208, 2016.
- Geoffrey E Hinton and S Zemel Richard. Autoencoders, minimum description length and Helmholtz free energy. In *Advances in Neural Information Processing Systems 6*, pages 3–10. Morgan-Kaufmann, 1994.
- Geoffrey E. Hinton, A. Krizhevsky, and S. Wang. Transforming auto-encoders. In *International Conference on Artificial Neural Networks*, pages 44–51. Springer, 2011.
- Lawrence Hubert and Phipps Arabie. Comparing partitions. *Journal of Classification*, 2(1):193–218, 1985.
- Sergey Ioffe and Christian Szegedy. Batch normalization: Accelerating deep network training by reducing internal covariate shift. In *32nd International Conference on Machine Learning*, pages 448–456, 2015.
- Sydney Jenkins, Elizabeth J Moyer, Ian Foster, Takuya Kurihana, Rebecca Willett, Michael Maire, Kathryn Koenig, and Ruby Werman. Developing unsupervised learning models for cloud classification. In *AGU Fall Meeting*, 2019.
- Chen Jin, Ruoqian Liu, Zhengzhang Chen, William Hendrix, Ankit Agrawal, and Alok Choudhary. A scalable hierarchical clustering algorithm using Spark. In *IEEE First International Conference on Big Data Computing Service and Applications*, pages 418–426. IEEE, 2015.
- Daeho Jin, Lazaros Oreopoulos, and Dongmin Lee. Simplified isccp cloud regimes for evaluating cloudiness in cmip5 models. *Climate Dynamics*, 48(1):113–130, 2017.
- S. C. Johnson. Hierarchical clustering schemes. *Psychometrika*, 32:241–254, 1967.
- Thomas Kluyver, Benjamin Ragan-Kelley, Fernando Pérez, Brian Granger, Matthias Bussonnier, Jonathan Frederic, Kyle Kelley, Jessica Hamrick, Jason Grout, Sylvain Corlay, Paul Ivanov, Damián Avila, Safia Abdalla, and Carol Willing. Jupyter notebooks – a publishing format for reproducible computational workflows. In F. Loizides and B. Schmidt, editors, *Positioning and Power in Academic Publishing: Players, Agents and Agendas*, pages 87–90. IOS Press, 2016.
- Takuya Kurihana. Rotation-Invariant Cloud Clustering code, 2022. <https://github.com/RDCEP/clouds>.
- Takuya Kurihana, Ian Foster, Rebecca Willett, Sydney Jenkins, Kathryn Koenig, Ruby Werman, Ricardo Barros Lourenco, Casper Neo, and Elisabeth Moyer. Cloud classification with unsupervised deep learning. In *9th International Workshop on Climate Informatics*, 2019.

- Takuya Kurihana, Elisabeth Moyer, Rebecca Willett, Davis Gilton, and Ian Foster. Data-driven cloud clustering via a rotationally invariant autoencoder. *IEEE Transactions on Geoscience and Remote Sensing*, pages 1–25, 2021. doi: 10.1109/TGRS.2021.3098008.
- Daniel D Lee and H Sebastian Seung. Learning the parts of objects by non-negative matrix factorization. *Nature*, 401(6755):788–791, 1999.
- Ravi Madduri, Kyle Chard, Mike D’Arcy, Segun C Jung, Alexis Rodriguez, Dinanath Sulakhe, Eric Deutsch, Cory Funk, Ben Heavner, Matthew Richards, et al. Reproducible big data science: A case study in continuous FAIRness. *PloS One*, 14(4):e0213013, 2019. doi: 10.1371/journal.pone.0213013.
- Willem J Marais, Robert E Holz, Jeffrey S Reid, and Rebecca M Willett. Leveraging spatial textures, through machine learning, to identify aerosols and distinct cloud types from multispectral observations. *Atmospheric Measurement Techniques*, 13(10):5459–5480, 2020.
- Tadashi Matsuo, Hiroya Fukuhara, and Nobutaka Shimada. Transform invariant auto-encoder. In *IEEE/RSJ International Conference on Intelligent Robots and Systems*, pages 2359–2364, 2017.
- AJ McDonald and Simon Parsons. A comparison of cloud classification methodologies: Differences between cloud and dynamical regimes. *Journal of Geophysical Research: Atmospheres*, 123(19):11–173, 2018.
- MODIS Characterization Support Team. Modis 1km calibrated radiances product, 2017a.
- MODIS Characterization Support Team. Modis 1km calibrated radiances product, 2017b.
- Veronica S Moertini, Gde W Suarjana, Liptia Venica, and Gede Karya. Big data reduction technique using parallel hierarchical agglomerative clustering. *IAENG International Journal of Computer Science*, 45(1), 2018.
- Nicholas Monath, Kumar Avinava Dubey, Guru Guruganesh, Manzil Zaheer, Amr Ahmed, Andrew McCallum, Gokhan Mergen, Marc Najork, Mert Terzihan, Bryon Tjanaka, Yuan Wang, and Yuchen Wu. Scalable hierarchical agglomerative clustering. In *27th ACM SIGKDD Conference on Knowledge Discovery and Data Mining*, pages 1245–1255, 2021.
- V. Nair and Geoffrey E. Hinton. Rectified linear units improve restricted Boltzmann machines. In *International Conference on Machine Learning*, 2010.
- Matthew R Norman, David A Bader, Christopher Eldred, Walter M Hannah, Benjamin R Hillman, Christopher R Jones, Jungmin M Lee, LR Leung, Isaac Lyngaas, Kyle G Pressel, Sarat Sreepathi, Mark A Taylor, and Xingqiu Yuan. Unprecedented cloud resolution in a gpu-enabled full-physics atmospheric climate simulation on olcf’s summit supercomputer. *The International Journal of High Performance Computing Applications*, 36(1):93–105, 2022. doi: 10.1177/10943420211027539.
- Preesan Rakwatin, Wataru Takeuchi, and Yoshifumi Yasuoka. Stripe noise reduction in MODIS data by combining histogram matching with facet filter. *IEEE Transactions on Geoscience and Remote Sensing*, 45(6):1844–1856, 2007.
- S. Rasp, H. Schulz, S. Bony, and B. Stevens. Combining crowd-sourcing and deep learning to understand meso-scale organization of shallow convection, 2019. ArXiv.
- Russ Rew and Glenn Davis. Netcdf: an interface for scientific data access. *IEEE computer graphics and applications*, 10(4):76–82, 1990.
- W. B. Rossow and R. A. Schiffer. ISCCP cloud data products. *Bulletin of the American Meteorological Society*, 71: 2–20, 1991.
- William B Rossow and Robert A Schiffer. Advances in understanding clouds from ISCCP. *Bulletin of the American Meteorological Society*, 80(11):2261–2288, 1999.
- William B Rossow, Alison W Walker, and Leonid C Garder. Comparison of ISCCP and other cloud amounts. *Journal of Climate*, 6(12):2394–2418, 1993.
- Peter J Rousseeuw. Silhouettes: A graphical aid to the interpretation and validation of cluster analysis. *Journal of Computational and Applied Mathematics*, 20:53–65, 1987.
- Jorge M Santos and Mark Embrechts. On the use of the adjusted Rand index as a metric for evaluating supervised classification. In *International Conference on Artificial Neural Networks*, pages 175–184. Springer, 2009.
- Tapio Schneider, Colleen M Kaul, and Kyle G Pressel. Possible climate transitions from breakup of stratocumulus decks under greenhouse warming. *Nature Geoscience*, 12(3):163–167, 2019.
- Alex Schuddeboom, Adrian J McDonald, Olaf Morgenstern, Mike Harvey, and Simon Parsons. Regional regime-based evaluation of present-day general circulation model cloud simulations using self-organizing maps. *Journal of Geophysical Research: Atmospheres*, 123(8):4259–4272, 2018.

- Bjorn Stevens, Sandrine Bony, H el ene Brogniez, Laureline Hentgen, Cathy Hohenegger, Christoph Kiemle, Tristan S L'Ecuyer, Ann Kristin Naumann, Hauke Schulz, Pier A Siebesma, et al. Sugar, gravel, fish and flowers: Mesoscale cloud patterns in the trade winds. *Quarterly Journal of the Royal Meteorological Society*, 146(726):141–152, 2020.
- Baris Sumengen, Anand Rajagopalan, Gui Citovsky, David Simcha, Olivier Bachem, Pradipta Mitra, Sam Blasiak, Mason Liang, and Sanjiv Kumar. Scaling hierarchical agglomerative clustering to billion-sized datasets, 2021. ArXiv.
- Bin Tian, M. K. Shaikh, M. R. Azimi-Sadjadi, T. H. Haar, and D. Reinke. A study of cloud classification with neural networks using spectral and textural features. *IEEE Transactions on Neural Networks*, 10:138–51, 1999.
- Robert Tibshirani, Guenther Walther, and Trevor Hastie. Estimating the number of clusters in a data set via the gap statistic. *Journal of the Royal Statistical Society: Series B (Statistical Methodology)*, 63(2):411–423, 2001.
- George Tselioudis, William Rossow, Yuanchong Zhang, and Dimitra Konsta. Global weather states and their properties from passive and active satellite cloud retrievals. *Journal of Climate*, 26(19):7734–7746, 2013.
- Ga el Varoquaux, Lars Buitinck, Gilles Louppe, Olivier Grisel, Fabian Pedregosa, and Andreas Mueller. Scikit-learn: Machine learning without learning the machinery. *GetMobile: Mobile Computing and Communications*, 19(1): 29–33, 2015.
- Ari Visa, Jukka Iivarinen, Kimmo Valkealahti, and Olli Simula. Neural network based cloud classifier. In *Industrial Applications of Neural Networks*, pages 303–309. World Scientific, 1998.
- Ulrike Von Luxburg. *Clustering Stability: An Overview*. Now Publishers Inc, 2010. doi: 10.48550/arXiv.1007.1075. ArXiv.
- Joe H Ward Jr. Hierarchical grouping to optimize an objective function. *Journal of the American Statistical Association*, 58(301):236–244, 1963.
- Mark D. Wilkinson, Michel Dumontier, IJsbrand Jan Aalbersberg, Gabrielle Appleton, Myles Axton, Arie Baak, Niklas Blomberg, Jan-Willem Boiten, Luiz Bonino da Silva Santos, Philip E. Bourne, Jildau Bouwman, Anthony J. Brookes, Tim Clark, Merc e Crosas, Ingrid Dillo, Olivier Dumon, Scott Edmunds, Chris T. Evelo, Richard Finkers, Alejandra Gonzalez-Beltran, Alasdair J.G. Gray, Paul Groth, Carole Goble, Jeffrey S. Grethe, Jaap Heringa, Peter A.C 't Hoen, Rob Hooft, Tobias Kuhn, Ruben Kok, Joost Kok, Scott J. Lusher, Maryann E. Martone, Albert Mons, Abel L. Packer, Bengt Persson, Philippe Rocca-Serra, Marco Roos, Rene van Schaik, Susanna-Assunta Sansone, Erik Schultes, Thierry Sengstag, Ted Slater, George Strawn, Morris A. Swertz, Mark Thompson, Johan van der Lei, Erik van Mulligen, Jan Velterop, Andra Waagmeester, Peter Wittenburg, Katherine Wolstencroft, Jun Zhao, and Barend Mons. The FAIR guiding principles for scientific data management and stewardship. *Scientific Data*, 3(1): 1–9, 2016.
- Robert Wood. Stratocumulus clouds. *Monthly Weather Review*, 140(8):2373–2423, 2012.
- World Meteorological Organization. International Cloud Atlas. <https://cloudatlas.wmo.int/>.
- Tianle Yuan, Hua Song, Robert Wood, Johannes Mohrmann, Kerry Meyer, Lazaros Oreopoulos, and Steven Platnick. Applying deep learning to nasa modis data to create a community record of marine low-cloud mesoscale morphology. *Atmospheric Measurement Techniques*, 13(12):6989–6997, 2020.
- Valentina Zantedeschi, Fabrizio Falasca, Alyson Douglas, Richard Strange, Matt Kusner, and Duncan Watson-Parris. Cumulo: A dataset for learning cloud classes. In *NeurIPS Workshop on Tackling Climate Change with Machine Learning*, 2019. <https://www.climatechange.ai/papers/neurips2019/11>.
- J. Zhang, Pu Liu, Feng Zhang, and Qianqian Song. CloudNet: Ground-based cloud classification with deep convolutional neural network. *Geophysical Research Letters*, 45:8665–8672, 2018.
- G. Zhao, L. Di Girolamo, D. J. Diner, C. J. Bruegge, K. J. Mueller, and D. L. Wu. Regional changes in earth's color and texture as observed from space over a 15-year period. *IEEE Transactions on Geoscience and Remote Sensing*, 54(7):4240–4249, 2016. doi: 10.1109/TGRS.2016.2538723.